Debes Bhattacharyya
Stoyko Fakirov

Synthetic Polymer-Polymer Composites

HANSER

Synthetic Polymer-Polymer Composites

Editors

DEBES BHATTACHARYYA and STOYKO FAKIROV 11
Center of Advanced Composite Materials, University of Auckland, New Zealand 12

ISBN (Book): 978-1-56990-510-4 16
ISBN (E-Book): 978-1-56990-525-8 17
HANSER PUBLISHERS, Munich 18

Chapter 14

Chapter 14

Preparation, Mechanical Properties and Structural Characterization of Microfibrillar Composites Based on Polyethylene/Polyamide Blends

Z. Z. Denchev, N. V. Dencheva

14.1. Introduction

An acceptable composite material for use in engineering applications should satisfy the following three basic requirements [1]: (i) to consist of at least two physically distinct and mechanically separable materials, which, depending on their properties and amounts used, are called *matrix* and *reinforcing component*; (ii) there must be a possibility for its preparation by admixing of the matrix and reinforcement components (sometimes preceded or accompanied by some special treatment so as to achieve optimum properties); and (iii) the final material is expected to possess several properties being superior to those of the individual components, *i.e.*, some synergistic effect should be present. The realization of this synergism requires strictly defined and reproducible distribution of the size and dispersion of the reinforcing component within the matrix, as well as a good adhesion and certain compatibility of the separate components forming the composite [2].

With respect to the size of the reinforcing component, polymer composites can be divided into three basic groups: (i) *macrocomposites*, comprising reinforcements with relatively large sizes (most frequently above 0.1 mm) of glass, carbon or some special rigid polymers; (ii) *nanocomposites*, where the reinforcements (typically inorganic) have at least one of their dimensions in the nanometer range (usually below or around 100 nm); and (iii) *molecular composites*, where the reinforcement is built up from single, rigid-rod macromolecules with diameters in the angstrom range. Based on the shape of the reinforcing entities, one can distinguish fibers (or one-dimensional), plate-like (two-dimensional) and powder-like (three-dimensional) fillers [3].

Examples of conventional macrocomposites are the fiber-reinforced systems consisting of an isotropic matrix made out of a polyolefin, polyamide, polyester, *etc*., that embeds organic or inorganic fibers of various lengths and arrangement with diameters typically larger than 1 μm. The fibers may be made of glass, carbon or Kevlar (Chapters 9 and 11). Good examples of nanocomposites are the carbon nanotube (CNT)-reinforced systems discussed in Chapters 3–8. Clay-reinforced polymer nanocomposites belong to the systems reinforced by two-dimensional fillers having significant importance in many industries and being the subject of numerous scientific publications [4–7]. A short review of the novel trends in polymeric nanocomposites was recently given by Mark [8].

With some approximation, liquid crystalline polymer (LCP) containing composites can be considered to be the closest example of molecular composites. By virtue of their molecular structure and conformation, the LCP reinforcements tend to form *in situ*, during processing, very fine fibers having similar or better reinforcing efficiency as compared to that of conventional inorganic fibers [9]. A substantial amount of work has also been performed in the area of LCP-containing composites described in numerous publications [10–13] and also in Chapters 12 and 13 of the present book.

About two decades ago, a new group of polymer materials was introduced, which became known as "microfibrillar composites" (MFCs) [14]. They can be considered to be a special type of fibril-reinforced composites that occupy an intermediate position between the macro- and nanocomposites in terms of the reinforcements' diameters, combining the easier processability of conventional polymer composites with the high aspect ratio (AR) of the LCP and CNT reinforcements typical of nano- and molecular composites. In MFC, a new production strategy was used, namely the *in situ* preparation of both matrix and fibril reinforcements [14,15]. These composites are obtained from properly chosen blends of thermoplastic polymers by a combination of appropriate mechanical and thermal treatments in three processing stages: melt-blending of the starting polymers, cold drawing of the blend followed by its selective isotropization at $T_1 < T < T_2$, where T_1 is the melting temperature of the lower-melting, matrix-forming component and T_2 is that of the highermelting one from which the reinforcing fibrils originate [16]. In other words, the MFC concept does not employ a starting nanomaterial to be blended with the matrix polymer, thus avoiding the general problems in nanocomposites technology, namely achieving proper dispersion of the reinforcing entities and not allowing their aggregation during processing [17]. The importance of the MFC materials for theory and for engineering practice has increased considerably during the last several years, although the major break-through in their industrial application has not yet occurred.

There exist several reviews related to the processing, properties, and morphology of MFCs produced from a number of polymer blends [16,18–23] that can be subdivided into two major groups. The first group comprises MFCs prepared

from a mixture of condensation polymers, *e.g*., polyester-polyamide, polyester-polycarbonate, polyester-poly(ether esters), *etc.* These blends are capable of *self-compatibilization* due to the so-called *interchange reactions* occurring between functional groups belonging to the matrix and reinforcements at their interface [24]. As a result, block copolymers are formed extending across the interface, thus linking the two MFC components chemically. In-depth studies on the interchange reactions in various blends of polycondensates and on the structure of the resulting copolymers have been performed, *e.g*., in poly(ethylene terephthalate)/ polyamide 6 (PET/PA6) [25], and PET/bisphenol A polycarbonate (PC) [26] blends, as well as in some other MFC precursors based on polycaprolactone/poly(2,2-dimethyltrimethylene carbonate) blends with possible medical applications [27]. For more details about the chemical interactions in a great variety of blends of polycondensates, the reader is encouraged to consult the reference literature [28,29]. In summary, the concrete nature of the interchange reactions depends on the chemical composition of the matrix and reinforcing materials and can occur as a polyesterification, polyamidation or ester–ester interchange requiring the typical conditions and catalysts for these specific reactions.

In polyolefin-containing MFCs that belong to the second group, the matrix does not possess the necessary chemical functionality so as to be bonded chemically to the respective reinforcing component; therefore, introduction of a compatibilizer is required. Among this group of MFC materials, most studied are the PET-reinforced matrices of high-density or low-density polyethylene (HDPE, LDPE) [30–37] and polypropylene (PP) [38–45]. The obvious reason for choosing PE and PP as matrix materials is related to their being cheap, abundant and easy to process. PET is preferred due to its inherent fiber-forming capability and to the fact that it is a major component of the plastics waste stream generated by the beverage industry. With this idea in mind, Evstatiev *et al.* [46] demonstrated the capability of MFC technology to improve the mechanical properties of LDPE and recycled PET blends. Later on, Taepaiboon *et al.* [47] studied the effectiveness of compatibilizers in improving the properties of the MFCs produced from blends of PP and recycled PET. Very recently, Lei *et al.* [48] employed MFC technology to make use of recycled HDPE and PET with the aid of compatibilizers.

Another group of polymers that has been considered widely as blend components in polyolefin-based blends are the polyamides (PA). They are known to have high water absorption, while PE and PP have low water absorption. In particular, HDPE has a stiffness near that of polyamide 6 (PA6) and polyamide 12 (PA12), which means that a blend should have a stiffness not too different from the starting components [49]. In addition, polyamides are engineering thermoplastics of high strength, good wear resistance and heat stability that makes them useful in the automotive industry, electrical equipment manufacturing and also in the textile industry. Blending of PE and polyamides provides a good way to make full use of their respective advantages [50]. This situation has led to many studies of blends of

HDPE and polyamides. The first systematic studies of Kamal *et al.* [51] on binary PE/PA immiscible blends incorporated three polyethylene resins (LDPE, linear low density polyethylene (LLDPE), and HDPE), and three polyamide resins (PA6, PA6,6, and chemically modified PA66). It was found that the mixing of PA into PE reduces the oxygen permeability while water vapor permeability is increased. These changes were the strongest in the HDPE-containing blends. Since PA and PE are immiscible, they tend to phase separate which results in poor mechanical properties. In order to achieve the desired combination between the good thermo-mechanical and oxygen barrier properties of PA and the high impact strength, easy processability and low cost of PE, it is necessary to use compatibilizing agents that will create chemical bonds across the interface. There exist many studies on the compatibilization of these blends [52–56]. Summarizing the results, it can be stated that the compatibilized blends had better mechanical properties than those for the non-compatibilized. Scanning electron microscopy (SEM) analysis showed that the addition of the compatibilizers significantly decreases the PA domains and improves the adhesion between PA and PE phases, which is probably the reason for improving the mechanical performance. Mechanical tests and SEM analysis also showed that there exist a number of compatibilizers that can be used in the blend compounding, representing various copolymers of polyethylene.

Surprisingly, there are only few studies on the possibility to use the MFC technology in PE/PA blends notwithstanding the good knowledge on the structure and properties of these blends. The main objective of this chapter is to summarize these studies in the field of the preparation, mechanical and structural characterization of HDPE/PA6 and HDPE/PA12 MFC materials. Along this presentation, the relationship between the mechanical properties and the structure of the MFCs on various length scales studied by various techniques will be discussed, as well.

14.2. Preparation and morphology of microfibrillar composites

The preparation of MFCs is quite different from that of the conventional composites, insofar as the reinforcing micro- or nanofibrils are created *in situ* during processing, as is the relaxed, isotropic thermoplastic matrix. The MFC technology can, therefore, be contrasted with the electro-spinning methods used to produce nano-sized materials mainly in the form of nonwoven fibers with colloidal length scales, *i.e.*, diameters mostly of tens to hundreds of nanometers [57]. As briefly stated above, the preparation of MFCs comprises three basic steps [16,19–23]. First, *melt-blending* is performed of two or more thermodynamically immiscible polymers with melting temperatures (*Tm*) differing by 30ºC or more. In the polymer blend so formed, the minor component should always originate from the higher-melting material and the major one from the lower-melting component

or could even be amorphous. Second, the polymer blend is drawn at temperatures equal or slightly above the glass transition temperatures (*Tg*) of both components leading to their molecular orientation (*fibrillation*). Finally, liquefaction of the lower-melting component is induced thus causing a nearly complete loss of orientation of the major component upon its solidification, which, in fact, constitutes the creation of the composite matrix. This stage is called *isotropization*. It is very important that during isotropization the temperature should be kept below *Tm* of the higher-melting and already fibrillated component. In doing so, the oriented crystalline structure of the latter is preserved, thus forming the reinforcing elements of the MFC. In the first studies on MFCs, the composites were prepared on a laboratory scale performing every one of the aforementioned three processing stages separately, one after another. Blending was done in a laboratory mixer or a single-screw extruder to obtain non-oriented strands that were afterward cold-drawn in a machine for tensile testing, followed by annealing of the oriented strands with fixed ends [14,15,58–60]. Obviously, this discontinuous scheme is difficult to apply in large-scale production. More relevant in this case are the continuous setups developed more recently [9,30,41,46, 61,62]. Blending of the components and extruding the oriented precursors could be performed in a twin-screw extruder coupled with water baths, heating oven and several cold stretching devices, as shown in Figure 14.1.

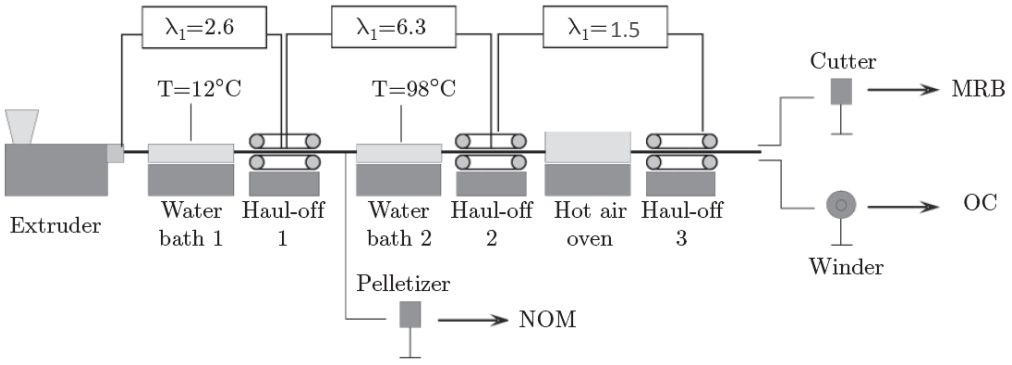

Figure 14.1 Schematic representation of the extrusion line used for preparation of polyethylene-polyamide MFC precursors: OC – oriented cable; MRB – middle-length, randomly distributed bristles; NOM – non-oriented material [61]

In the particular case of HDPE/PA6 and HDPE/PA12 precursor materials, the procedures were as followed [63,64]. Granulates of PA6 or PA12 (pre-dried for 6 h at 100ºC), HDPE and compatibilizer (a copolymer of HDPE-maleic anhydride (MAH) commercially available under the name Yparex, YP) were premixed in a tumbler in the desired proportions. Each mixture was introduced into a gravimetric

feeder that fed it into the hopper of a Leistritz LSM 30.34 laboratory intermeshing, corotating twin-screw extruder. The extruder screws rotated at 100 rpm, and the temperature in its 8 sections was set in the range of 240–250 (for HDPE/PA6) and at 230ºC (for the HDPE/PA12 blends). The resulting extrudate was cooled in the first water bath at 12ºC. Meanwhile, the first haul-off unit applied a slight drawing to stabilize the extrudate crosssection. Further drawing was performed in the second haul-off unit after the strand passed through the second water bath heated to 97–99ºC. A third haul-off unit applied the last drawing, causing the diameters to decrease from 2 mm (at the extruder die) to approximately 0.6–0.9 mm at the end of the extruder line. Thus, twelve oriented HDPE/PA/YP blends with compositions given in Table 14.1 were obtained initially in the form of continuous oriented cables. These cables were then cut to shape and compression molded at a temperature below the melting point of the respective reinforcing polyamide into three MFC types: (i) in the form of orthotropic laminae obtained from unidirectional plies of cables (UDP), (ii) cross-ply laminates (CPC) obtained from two plies of oriented cables arranged perpendicularly, and (iii) composites from middle-size randomly distributed PA6 bristles (MRB). Compression molded non-oriented pellets obtained right after extrusion and denoted as "non-oriented material" (NOM) were also produced from each blend and tested for comparison. Figure 14.2 shows the visual aspect of various types of precursors. Figure 14.3 depicts the preparation of the CPC laminates from two perpendicularly aligned unidirectional plies of oriented cables but the form and dimensions are valid for all composite types. It is worth mentioning that compression molding (CM) is not the only way to transform the oriented precursors into fibrillar micro- or nanostructured composites.

Table 14.1. Composition of the HDPE/PA/YP composites. From each composition UDP, CPC, MRB and NOM composites were produced [69]

HDPE/PA/YP composite designation	HDPE (wt%)	PA (wt%)	YP (wt%)
90/10/0	90.0	10.0	0
80/20/0	80.0	20.0	0
70/20/10	70.0	20.0	10.0
75/20/5	75.0	20.0	5.0
77.5/20/2.5	77.5	20.0	2.5
65/30/5	65.0	30.0	5.0

Notes: PA = PA6 or PA12; YP – HDPE-MAH copolymer commercially available from DSM as Yparex; UDP – MFC lamina obtained from continuous oriented cables arranged in the form of unidirectional ply; CPC – MFC laminate obtained from cross-ply arranged oriented cables; MRB – MFC obtained from middle-length randomly distributed bristles; NOM – composite obtained from non-oriented mixture.

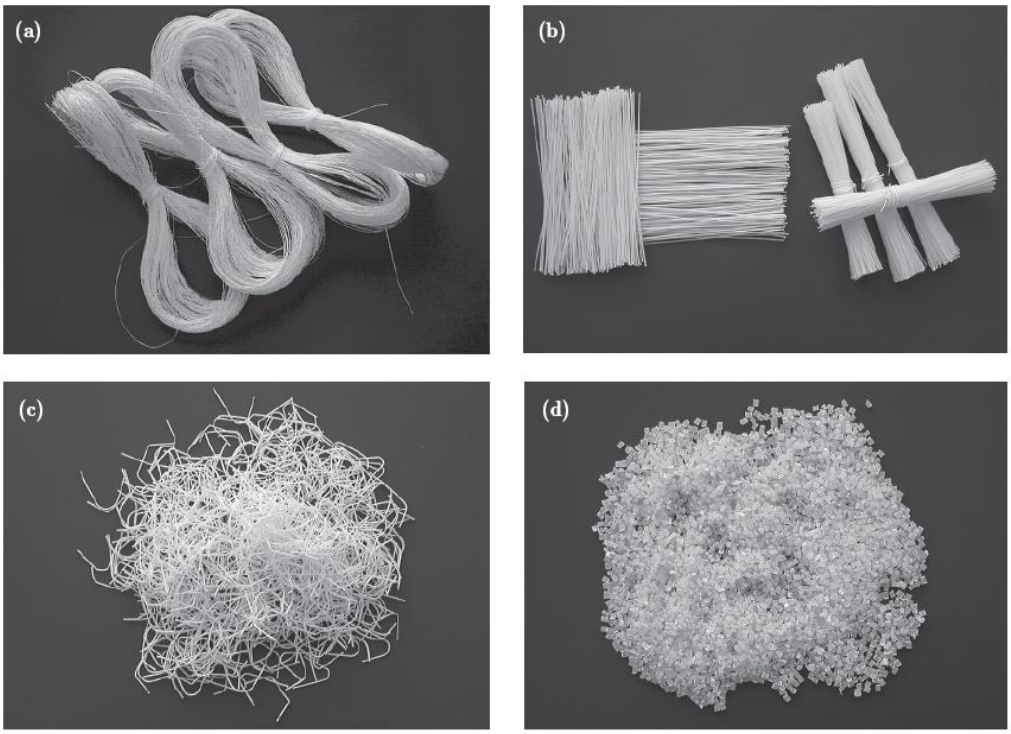

Figure 14. 2. Various MFC precursors obtained after the homogenization and cold drawing stages; (a) OC – oriented cable after the 3rd haul-off; (b) bundles of cut bristles with parallel orientation of the fibers' axes; (c) MRB – middle-length randomly distributed bristles; and (d) NOM – non-oriented material obtained by palletizing the extrudate before the first haul-off [63]

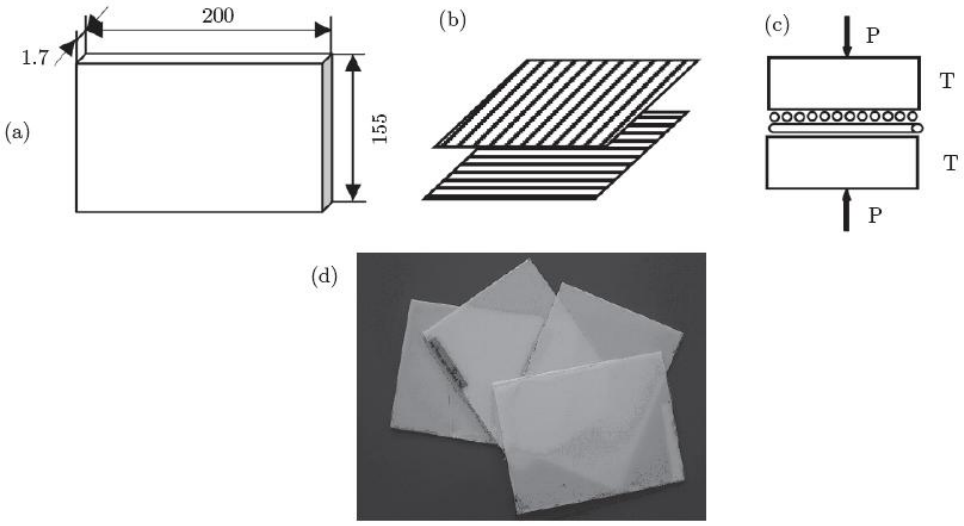

Figure 14..3. Preparation of the cross-ply laminates (CPC): (a) dimensions of composite plates, mm; (b) two unidirectional plies of oriented precursors, perpendicularly aligned; (c) compression molding at temperature T=160°C, and pressure, p=1.5 MPa; and (d) visual aspect of the resulting laminate plates used for flexural and impact resistance tests [69]

Chopping the continuous OCs into pellets allows their reprocessing into MFC by extrusion or by injection molding (IM). This alternative was reported by Monticciolo *et al.* for PE/poly(butylenes terephthalate) blends [65] and was followed later by other authors [33,46] with PET/HDPE blends. Both CM and IM matrix isotropization have been used in PET-reinforced PA6 MFCs [9] showing an improvement of the mechanical performance as compared to that of the neat PA6 matrix. According to this work, the CM approach allowed to stay more accurately within the necessary processing temperature window and to preserve better during the isotropizaton stage the microfibrillar morphology of PET. For this reason, the mechanical properties in impact and flexural mode were better. On the other hand, one should bear in mind that in contrast to CM, IM cannot produce laminates with continuous and parallel reinforcing fibrils, by which the advantages of the MFC technology are most obvious.

A possibility to avoid the CM stage is offered by the modified method for preparation of *in situ* MFCs based on consecutive slit or rod extrusion, hot stretching and quenching [32,37,38,42,43,47,62] used to process thermoplastic polymer blends, mostly polyolefins and PET. Rotational molding of LDPE/PET beads has also been attempted for the same purpose [34], but the reinforcing effect was insufficient due to the uneven distribution of the reinforcing fibrils and also due to their reversion to spheres, losing their MFC structure in this particular case.

An interesting further development of the MFC preparation concept is found in [66]. A PP/PET blend is prepared by melt extrusion which is thereafter spun into textile synthetic fibers followed by knitting or weaving and the obtained fabric is compression molded at 180ºC, *i.e.*, below the melting point of the PET reinforcement. Apart from the observed 50% increase of the Young's modulus, some 20% enhancement of the tensile strength was found, which is typical for the polymer nanocomposites to which the prepared material belongs. In addition, the authors describe the preparation of nanofibrillar fabrics by means of a simple selective dissolution of the matrix PP with possible applications for scaffolds and *single-polymer composites*, SPC (Chapter 27).

14.3. Mechanical characterization of PE/PA microfibrillar composites

It is generally accepted [16] that the mechanical properties of the MFC with optimized composition made under best processing conditions are superior to those of the corresponding neat matrix material due to the high aspect ratio (AR) of the crystalline and oriented microfibrillar reinforcement, and in view of the various possibilities to strengthen the matrix–fibril interface by compatibilization or transcrystallization. All of the systematic mechanical studies on MFC were made with systems based on polyolefin matrices reinforced by PET microfibrils and no such studies are available for PE/PA MFC systems.

Thus, MFCs obtained from LDPE/PET oriented blends selectively isotropized by injection molding achieved elastic moduli approaching those of LDPE + 30% glass fibers (GF). The tensile strength of MFCs has reached at least two times that of the neat LDPE matrix material, the impact strength of the MFC being 50% higher [30]. Extensive mechanical studies have also been performed with the PP/PET [44], LDPE/PET [46] and HDPE/PET MFCs [36,67]. The tribological properties of polyolefin matrices reinforced by PET or PA6,6 were also studied [68]. It was established that the reinforcement with PA6,6 fibrils leads to higher wear resistance in comparison to PET in MFC with the same matrix material. The wear rates were found to be much lower in MFC with uniaxially oriented reinforcing fibrils as compared to materials with random orientation of the reinforcements.

In this chapter results from the tensile, flexural and impact tests on HDPE/PA6 and HDPE/PA12 MFC are presented studying the effects of the compatibilizer, HDPE and PA concentration, as well as the form and arrangement of the reinforcing entities on the mechanical behavior. The UDP MFC laminae were used for tensile tests. Impact strength and three-point flexural tests were performed on the CPC laminates. MRB and NOM composites were analyzed with the three mechanical tests. The data were compared with those of the neat HDPE matrix material and/or the oriented polyamide component [69].

14.3.1. *Tensile tests with HDPE/PA6 systems*

The anisotropic UDP lamina represents the basic building block in composites reinforced by long fibers. Knowing its tensile properties allows their modeling for any kind of laminate composites, produced from two and more such laminae [70]. The tensile tests were performed under the conditions indicated in [69]. An Instron 4505 testing machine was used operating at constant crosshead speed of 50 mm/min. From each UDP laminae test samples in two mutually perpendicular directions were cut out. The nominal stress was determined as the ratio of the tensile force and the initial cross-section of the sample. The nominal strain was determined as the ratio of the sample gauge length at any time during drawing and that prior to testing. The Young's moduli were calculated from the stress-strain curves at 1% strain (secant modulus). For each UDP MFC sample, two experimental values for the Young's modulus E and the ultimate strength σ_{max} were obtained: longitudinal (E_1, σ_{1max}) and transverse (E_2, σ_{2max}). Theoretical predictions for these parameters were calculated as suggested in [70]. Equation (14.1) was used for the E_1 values:

$$E_1 = V_f E_f + E_p(1 - V_f) \approx V_f E_f \qquad (14.1)$$

where E_p and E_f are the respective moduli of the matrix and of the fibers, and V_f is the volume fraction of fibers (*the rule of mixtures*).

The transverse modulus E_2 estimates were derived from Equation (14.2):

$$\frac{1}{E_2} = \frac{V_f}{E_f} + \frac{1 - V_f}{E_p}$$

The longitudinal tensile strength of the UDP composites was estimated approximately by (14.3):

$$\sigma_{1\max} = \sigma_{f\max} \cdot V_f$$

where $\sigma_{1\max}$ is the strength of the PA6 oriented fiber.

In the transversal direction it is assumed that (14.4):

$$\sigma_{2\max} = 0.33\sigma_{p\max},$$

where $\sigma_{p\max}$ is the tensile strength of the matrix.

Figure 14.4 shows some typical stress-strain curves of HDPE/PA6 unidirectional ply MFCs in the longitudinal direction. The 90/10/0 composition containing 10 wt% PA6 displays a ductile behavior similar to the HDPE matrix. In the two corresponding curves there exist clear yielding and necking, even though the strain at break ε_{br} of the composite (about 100%) is much smaller than the HDPE alone (about 800%). The other stress-strain curves show the typical brittle behavior of composite materials, with εbr not exceeding 30–40%, and σ1max considerably higher than the matrix. Similar curves were obtained when stretching in a direction transversal to the fiber axis.

The reinforcing effect in the UDP MFC was assessed on the basis of the E and σmax data from the stress-strain curves in comparison with the data of the neat HDPE matrix, or the model predictions based on Equations (14.1)–(14.4).

Table 14.2 shows the absolute values of the longitudinal Young's modulus E1 and the ultimate strength σ1max of HDPE/PA6/YP UDP MFC and their relative increases with respect to the HDPE matrix. All MFC compositions show an improvement of E_1 in the 11–33% range, the biggest being for composites without compatibilizer and the smallest for the composition with 10% of Yparex. The σ1max for all composites grow significantly reaching approximately 60 MPa for the 80/20/0 MFC or a 120% of improvement in respect to HDPE. Again, the MFCs with the biggest concentration of compatibilizer showed the smallest enhancement of the tensile strength. Similar influence of the compatibilizer has been observed in

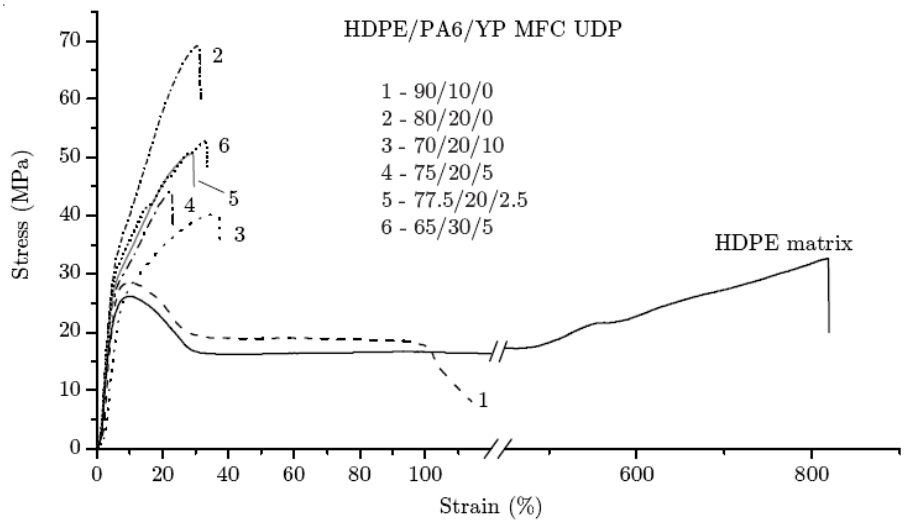

Figure 14.4. Representative stress-strain curves of HDPE/PA6/YP UDP MFCs. For comparison, the curve corresponding to the HDPE matrix is also shown [69]

Table 14.2. Absolute values of the longitudinal Young's modulus, E_1, and the ultimate strength, σ_{1max}, of HDPE/PA6/YP UDP MFCs and their relative increases in respect to the HDPE matrix [69]

Composition HDPE/PA6/YP (wt%)	E_1 (MPa)	ΔE_1 (%)	σ_{1max} (MPa)	$\Delta\sigma_{1max}$ (%)
100/0/0	827±47	0	26±1	0
90/10/0	940±21	13.7	27±1	3.8
80/20/0	1095±52	32.4	57±4	119.2
70/20/10	920±7	11.2	37±2	42.3
75/20/5	961±19	16.2	45±3	73.1
77.5/20/2.5	1030±19	24.5	45±3	73.1
65/30/5	1098±48	32.8	52±8	100.0
0/100/0 oriented	1830±31	–	230±7	–

Notes: $\Delta E_1 = (E_1 - E_{HDPE}).100/E_{HDPE}$; $\Delta\sigma_1 = (\sigma_1 - \sigma_{1HDPE}).100/\sigma_{1HDPE}$

isotropic HDPE/PA6 blends in the presence of MAH-g-PP copolymer [71]. The authors relate this effect to the low molecular weight of the compatibilizer located

Table 3. Longitudinal and transversal tensile properties of UDP MFCs with various compositions and their relative changes in respect to the predicted values [69]

Composition HDPE/PA/YP, (wt%)	Vol. fract. of PA6, (V_f)	E_1 (MPa)	ΔE_1 (%)	E_1^* (MPa)	σ_{1max} (MPa)	$\Delta\sigma_{1max}$ (%)	σ_{1max}^* (MPa)	E_2 (MPa)	ΔE_2 (%)	E_2^* (MPa)	σ_{2max} (MPa)	$\Delta\sigma_{2max}$ (%)
100/0/0	–	827±47	0	–	26±1	0	–	851±32	0	–	27.0±0.4	0
90/10/0	0.084	940±21	3.2	911	27±1	42.1	19	962±65	11.0	867	25.1±1.0	181.7
80/20/0	0.171	1095±52	9.6	999	57±4	46.2	39	630±77	–31.0	913	12.6±0.5	41.4
70/20/10	0.171	920±7	–7.8	998	37±2	–5.1	39	840±27	–8.0	913	21.4±0.3	140.2
75/20/5	0.171	961±19	–3.7	998	45±3	15.4	39	870±15	–4.7	913	17.0±1.3	90.8
77.5/20/2.5	0.171	1030±19	3.2	998	45±3	15.4	39	855±24	–6.4	913	21.2±1.2	137.9
65/30/5	0.261	1098±48	0.8	1089	52±8	–13.3	60	323±20	–66.5	965	3.7±0.4	–58.5
0/100/0 (oriented)	–	1830±31	–	–	230±7	–	–	–	–	–	–	–

Notes: E_k^* and σ_{kmax}^* (k=1,2) are the theoretical values derived from Eqs. (??.1)–(??.4);
$\Delta E_k = (E_k – E_k^*)*100/E_k^*$; $\Delta\sigma_1 = (\sigma_k – \sigma_{kmax}^*)*100/\sigma_{kmax}^*$;
$\sigma_{2max}^* = 0.33\,\sigma_{pmax} = 8.91$ MPa, wherein σ_{pmax} is the tensile strength of HDPE in transverse direction.

at the interface between the two components and acting as a mechanically weak boundary phase. We will come back to this issue in the next section of this chapter.

Table 14.3 summarizes the experimental Young's moduli and tensile strength data of all HDPE/PA6/YP compositions in the longitudinal and transverse directions and their relative changes with respect to the predictions using Eqs. (14.1)–(14.4). Comparing the predicted and experimental longitudinal E_1 and σ_{1max} data, it can be concluded that the rule of mixtures describes well all HDPE/PA6/YP UDP MFC. The experimental values are close and sometimes higher than predicted, the lower the amount of compatibilizer, the bigger the difference. For example, the 80/20/0 system shows the largest positive deviation with ΔE_1 of *ca.* 10%, while the experimental E_1 of the 70/20/10 composition is smaller than the calculated one with a negative deviation of *ca.* 8%. The $\Delta\sigma_{1max}$ data show the same trend, the non-compatibilized MFCs displaying the biggest positive deviation in the range of 42–46%.

As seen from Table 14.3, the tensile properties of the HDPE/PA6/YP UDP MFC in the transverse direction do not follow the rule of mixtures. Most of the E_2 values are lower than the predictions and are close to HDPE. The 90/10/0 composition is the only one that shows a positive deviation from the theoretical value. As regards σ_{2max}, it is significantly higher than the expected value of 0,33.σ_{2max} of HDPE. The positive deviations vary from 46% for the 80/20/0 to 180% for the 90/10/0 composition. An exception to this trend is the 65/30/5 MFC with very low experimental E_2 and σ_{2max} data. It is to be noted that the 90/10/0 laminae display satisfactory tensile properties also in the transversal direction, showing a Young's modulus *ca.* 11% higher than E^*_2 and experimental tensile strength 180% higher than σ^*_{2max}. The fact that in transversal direction there are also deviations from the values expected by the theory of the long fiber-reinforced composites suggests that the respective explanations should be related to the unique structure and morphology of the MFC.

The data in Tables 14.2 and 14.3 allow the conclusion that in order to improve the longitudinal tensile properties of UDP MFC, no compatibilizer or very small amounts of it should be implemented. Compatibilization, however, is needed for better mechanical performance in the UDP MFC in transverse direction and also to enhance the cold drawing processing stage. In addition, both E_1 and σ_{1max} of most UDP MFC are higher than predicted using the rule of mixtures. A possible explanation is that the reinforcing PA6 fibrils in the UDP MFC are stiffer and stronger and with larger AR than in the oriented PA6 samples used to calculate the theoretical E and σ. (See next section.)

Table 14.4 summarizes tensile test data for HDPE/PA6/YP MRB and NOM composites. It can be seen that the Young's moduli and strengths in longitudinal and transverse directions of the MRB MFC are close to one another. Most of the compositions show some improvement in tensile performance as compared to HDPE. The E and σ values, however, remain clearly below those of the UDP

lamina in the longitudinal direction. This confirms that the alignment of the fibrils is of major importance for the tensile properties in MFC. Considering the tensile properties of the NOM composites (Table 14.4), one should bear in mind that the HDPE matrix is reinforced by microspheres of PA6, similarly to the glass sphere reinforced composites. NOM composites are not MFC, since the reinforcing constituent is not fibrillar. The 70/20/10 NOM displays considerable improvement of both Young's modulus and tensile strength. This is contrary to what was observed in the respective UDP, where the 70/20/10 composition showed the poorest tensile performance. At this point, a supposition can be made that when the PA6 is isotropic a better compatibilization can be achieved improving the adhesion at the HDPE/PA6 interface. Another remark is that the 90/10/0 NOM system also displays enhanced modulus values. This was not the case with the conventional melt blended HDPE/PA6 system [71], where a minimum of 20% of PA6 was necessary to achieve some improvement of the tensile properties. The difference can be attributed to the specific processing conditions of the NOM composites, namely to the fact that the matrix isotropization was done at 160ºC, *i.e.*, far below the PA6 melting point. In such a way PA6 undergoes annealing that leads to higher crystallinity and increase of the α-PA6 polymorph content, resulting in higher tensile modulus. Similar effects were observed with isotropic and oriented PA6 samples annealed at 160ºC [72,73].

Figure 14.5 shows a direct comparison of the longitudinal tensile properties of all the UDP, MRB and NOM composites as a function of their HDPE/PA6/YP composition. It can be seen (Figure 14.5a) that almost all of the composites display E_1 higher than HDPE, the only exception being the 65/30/5 system, where only the UDP lamina shows improved tensile stiffness. In the case of the 90/10/0 composites, there is no statistically significant difference between the moduli of UDP, MRB and NOM, *i.e.*, the type of PA6 reinforcement (fibrillar or isotropic) and the alignment of the fibrils do not influence the stiffness. Considering the compositions with 20% PA6, one can assess the influence of these two parameters, as well as that of the compatibilizer. Clear enhancement of the modulus is registered only where the reinforcements are aligned fibrils – in the UDP laminae. Within the 20% PA6 series, high moduli are observed either without or at low YP concentrations. When the reinforcing component is isotropic (NOM), the trend is inversed. In this case, the higher compatibilizer concentration favors the stiffness. Apparently, the compatibilizing effect is better expressed when the PA6 reinforcement is isotropic.

Table 14.4. Longitudinal and transversal tensile properties of MRB and NOM composites [69]

HDPE/PA6/YP (wt%)	Vol. fract. of PA6, (V_f)	E_1 (MPa)	E_2 (MPa)	σ_{1max} (MPa)	σ_{2max} (MPa)
		HDPE/PA6/YP MRB MFC			
100/0/0	–	827±47	851±32	26±1	27±1
90/10/0	0.084	899±43	926±46	24.±.1	23±1
80/20/0	0.171	903±54	904±47	24±6	22±3
70/20/10	0.171	854±25	891±7	25±1	25±1
75/20/5	0.171	898±70	889±65	29±4	25±1
77.5/20/2.5	0.171	886±34	960±36	31±5	24±3
65/30/5	0.261	744±50	722±31	16±2	12±1
0/100/0 (oriented)	–	1830±31	–	230±7	–
		HDPE/PA6/YP NOM			
100/0/0	–	827±47	851±32	26±1	27±1
90/10/0	0.084	906±53	906±35	24±1	25±1
80/20/0	0.171	871±47	869±52	22±1	21±3
70/20/10	0.171	973±45	1028±4	29±1	31±1
75/20/5	0.171	923±10	986±33	22±2	21±2
77.5/20/2.5	0.171	884±75	893±46	22±1	22±2
65/30/5	0.261	772±59	712±43	11±1	9±1
0/100/0 (isotropic)	–	1110±40	1080±35	51±2	50±1

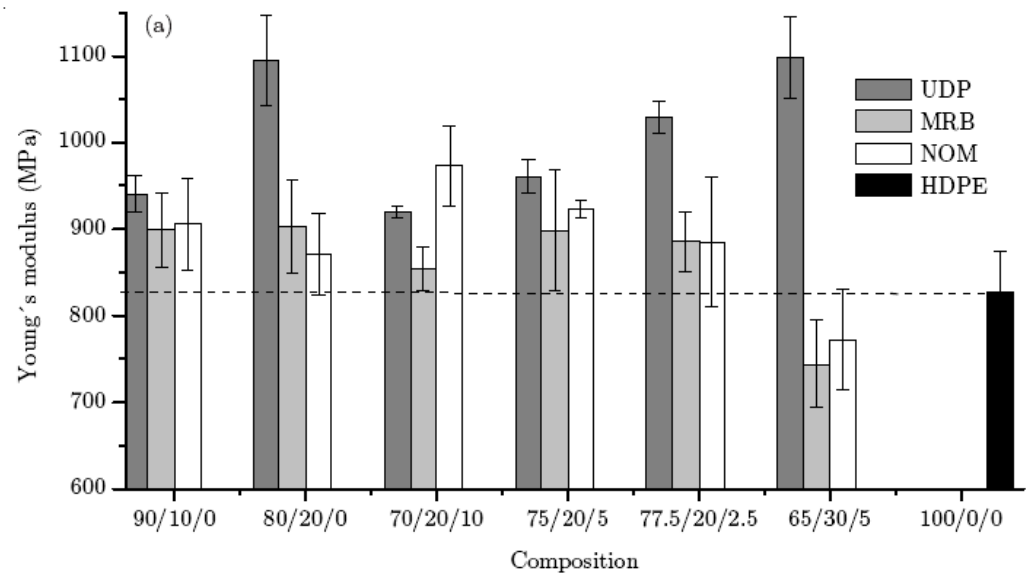

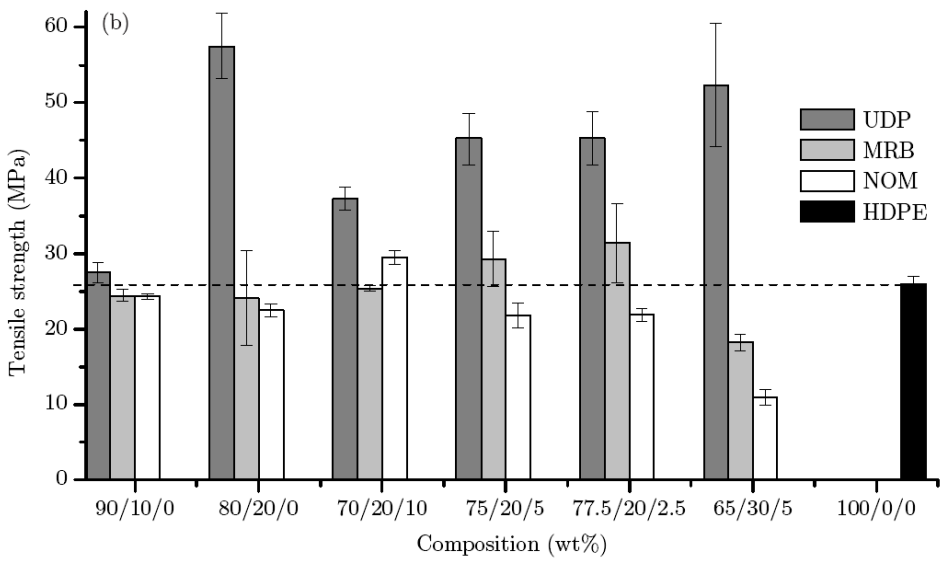

Figure 14. 5. Longitudinal tensile properties of HDPE/PA6/YP UDP, MRB and NOM composites and the HDPE matrix: (a) E_1, and (b) σ_{1max} [69]

As far as the tensile strength values are concerned (Figure 14.5b), a clear increase of σ1max is observed only in the UDP MFC. The compatibilizer concentration influences the strength in the same way as the stiffness. The systems without compatibilizer show an improvement of σ1max of above 100%. In the isotropic MRB and NOM composites, the strength data are close or even worse than those of the matrix. Therefore, to obtain *in situ* MFC of higher strength and stiffness one should consider the preparation of laminates with several UDP.

14.3.2. *The flexural tests*

In practice, in very few cases materials work in tensile mode, more often they are subjected to flexure or impact. On the other hand, fiber-reinforced composites are usually applied as laminates with different orientation and alignment of the fibrous reinforcement. That is why the CPC laminates were used to study their flexural stiffness and impact resistance.

The flexural tests were performed by the 3-point support test method used by Nunes *et al.*, as shown in Figure 14.6 [74]. The support was mounted in the same Instron machine used for the tensile tests this time operating in compression mode. Rectangular samples (155×100 mm) were cut out from the CPC MFC plates and placed upon the support.

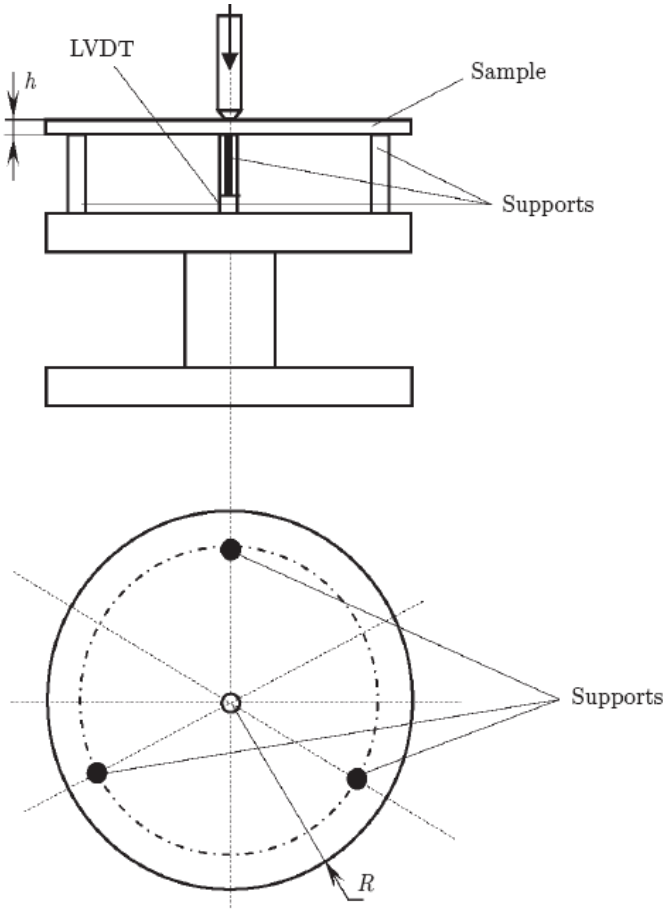

Figure 14.6. Schematic diagram of the three-point support flexural test: h – sample thickness, LVDT – Linear Variable Differential Transformer displacement transducer, $R = 46.75$ mm [69]

A maximum load of 1 kN was applied at the centre of the sample using a crosshead speed of 5 mm/min. From the force-displacement curves the slope *Sp* was determined and used to calculate the reduced flexural stiffness *CR* [74]:

$$C_R = \frac{3}{2\pi h^3} R^2 S_p \qquad (14.5)$$

In this equation, *h* is the sample thickness varying in the 1.4–1.8 mm range and *R* = 46.75 mm is the radius of the circumference on which the three supports are located. Eight samples of each CPC, MRB and NOM laminates were tested. Similar measurements were performed with the neat HDPE and the improvement factor, *IF*, was calculated as:

$$IF = \frac{C_R^{Comp} - C_R^{Matrix}}{C_R^{Matrix}}.100, \% \quad (15.6)$$

In the other works where the 3-point support test was used [74,75], circular test specimens were tested. In this study rectangular plates were used instead. To assess the deviations introduced by these geometries with respect to the theoretical test geometry, simulations with the ABAQUS software [76] were performed with two forces (1 kN and 100 N). The output of these simulations is presented in Figure 14.7. Based on this, it is possible to conclude that using rectangular plates instead of overhanging circular plates has a negligible effect on the results.

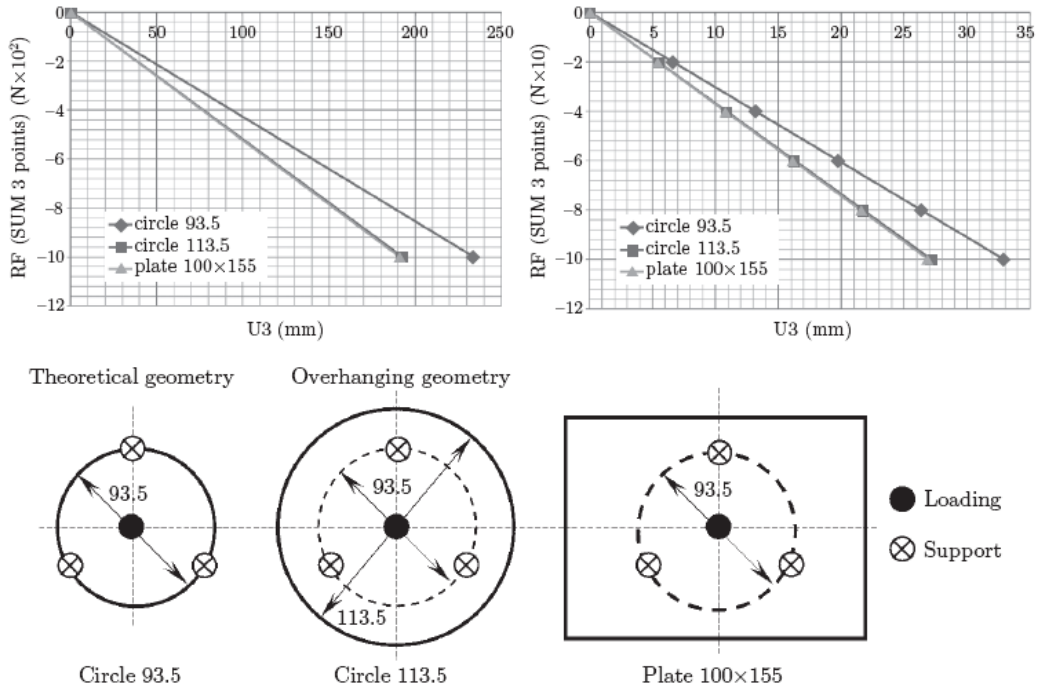

Figure 14. 7. Simulation results obtained with the ABAQUS software with two circular and one rectangular test specimens subjected to three-point-support flexural tests [69]

The flexural data for HDPE/PA6/YP CPC MFC are summarized in Table 14.5. All composites show a notable improvement of the flexural performance with C_R values of 2.3–2.6 GPa, *i.e.*, well above the HDPE matrix value of 1.5 GPa. Thus, for the CPC laminates the *IF* varies between 55% for 70/20/10 system to 78% for 80/20/0, whereby increasing the concentration of YP resulted in smaller C_R. The 80/20/0 CPC MFC shows the higher increase of C_R. The same system as a UDP lamina had the best performance in tension too, with improvements in the Young's modulus and tensile strength of 10 and 46%, respectively. In the HDPE/PA6/YP

MRB series it is the 65/30/5 composition that shows the highest C_R. This seems to be related to the largest amount (30%) of randomly arranged short PA6 reinforcing fibrils. Within the MRB samples containing 20% PA6 the composition with 10% compatibilizer displays unusually good flexural characteristics**.** Similarly to the CPC and MRB, all NOM compositions also showed better performance than the HDPE matrix.

Table 14.5. Flexural properties of HDPE/PA6/YP CPC, MRB and NOM composites [69]

Composition HDPE/PA6/YP (wt%)	Slope S_p (N/mm)	Average thickness (mm)	Flexural stiffness CR (GPa)	Improvement factor (%)
100/0/0	11.361	2.002	1.478 ± 0.057	0
		HDPE/PA6/YP CPC		
90/10/0	11.844	1.705	2.493±0.148	69
80/20/0	17.262	1.893	2.624±0.245	78
70/20/10	11.366	1.730	2.294±0.224	55
75/20/5	12.868	1.736	2.564±0.146	73
77.5/20/2.5	13.543	1.758	2.595±0.109	76
65/30/5	14.621	1.823	2.516±0.191	70
		HDPE/PA6/YP MRB		
90/10/0	12.946	1.774	2.425±0.182	64
80/20/0	15.524	1.916	2.302±0.148	56
70/20/10	13.198	1.766	2.503±0.051	69
75/20/5	13.370	1.845	2.216±0.175	50
77.5/20/2.5	12.559	1.791	2.282±0.085	54
65/30/5	16.800	1.862	2.723±0.376	84
		HDPE/PA6/YP NOM		
90/10/0	12.365	1.736	2.464±0.110	67
80/20/0	11.448	1.740	2.267±0.176	53
70/20/10	10.521	1.710	2.198±0.098	49
75/20/5	11.042	1.719	2.271±0.024	54
77.5/20/2.5	11.192	1.719	2.301±0.072	56
65/30/5	18.919	2.017	2.408±0.138	63

As seen from the comparison in Figure 14.8, there is no statistically significant difference in the flexural stiffness data of CPC, MRB and NOM composites, especially in samples containing 10% of PA6. This means that for the flexural properties it does not really matter if the reinforcement is isotropic or oriented. The

alignment of the PA6 fibrils does not seem to be important in this case either. It should be pointed out that only 10% of PA6 is sufficient to impart a notable flexural stiffness to the HDPE matrix, the improvement being in the range of 60–70%.

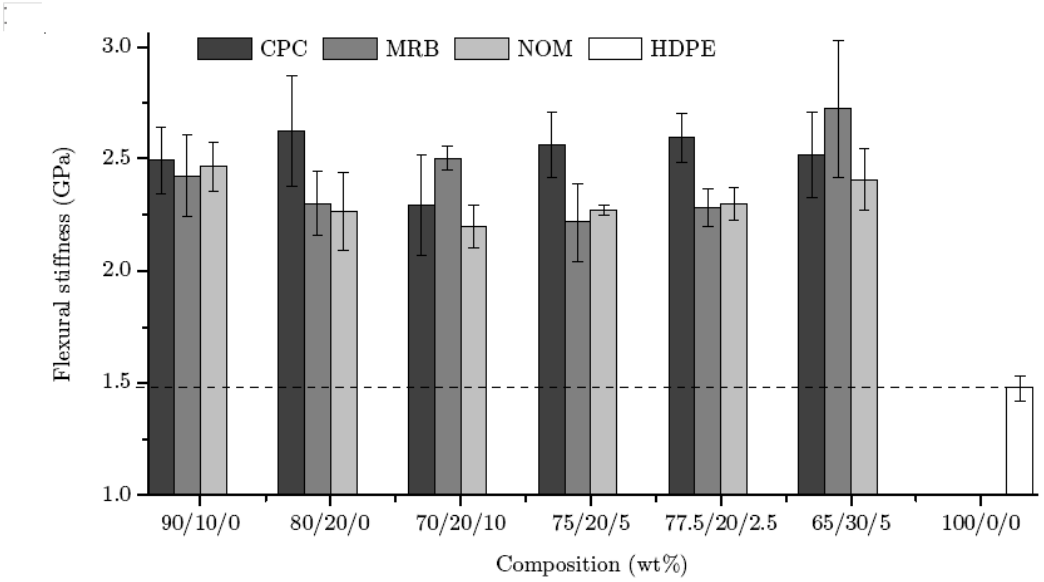

Figure 14.8. Comparative chart of the flexural stiffness of all HDPE/PA6/YP composites studied [69]

Higher improvement factors of 70–80% were observed in the CPC laminates containing 20% PA6, in the absence or at low concentration of the YP compatibilizer. The increase of the YP concentration up to 10% causes deterioration of the flexural behavior of the CPC composites. The composition with 30% PA6 also leads to an improvement in the flexural properties comparable to that with 20% reinforcement.

14.3.3. *The impact tests*

The impact tests were carried out using a CEAST Fractovis instrumented falling weight impact tester. The test samples were square plates of 60×60mm machined from the respective compression molded plates. Eight impact samples of each material were impact tested at –40ºC, the cooling being achieved by a mixture of liquid nitrogen and petroleum ether. The samples were impacted using a drop height of 1 m, leading to an impact speed of approximately 4.4 m/s. The force experienced by the sample as a function of time was determined. Assuming a constant impact speed, time was recalculated as displacement. From the force *versus* displacement graphs, peak force, peak energy and total energy were determined. In each test, the values for peak and total energy were divided by the

sample thickness to give the specific energy per millimeter thickness. The latter values were considered as peak and total impact strengths, respectively, as suggested by Pick *et al.* [77].

The peak and total energies per thickness for all sample types are represented in Figure 14.9 as a function of the composition. In the case of CPC and MRB MFCs where the reinforcement is fibrillar, (Figures 14.9a and b), the peak impact energy is lower than for HDPE. The total impact energy, however, is much higher than of the matrix. This means that in CPC and MRB the failure starts at lower energy levels, but the crack propagation before the total failure requires more energy. It can be noted that the 80/20/0 and 77.5/20/2.5 CPC composites require a considerable increase of the total energy, while their peak energies are only slightly above the matrix. It seems that 20% of PA6 is the optimal concentrations in CPCs and MFCs; increasing the PA6 component to 30% has a negative effect and keeping it as low as 10% is not enough, as far as the peak energy is concerned. It is noteworthy that the total impact strength is quite sensitive to the YP content, decreasing as YP increases. These findings agree with the tensile studies, where the MFC containing 20% of PA6 without or with minimum amount of YP performed the best. The NOM composites where the reinforcing PA6 entities are globular show impact characteristics significantly lower than the HDPE matrix (Figure 14.9c). Hence, it is the fibrillar morphology of the PA6 component in CPC and MRB composites that favors the impact properties.

14.3.4. *A comparison between the mechanical properties of PA6 and PA12 MFCs*

The mechanical properties of the HDPE/PA12 compatibilized and non-compatibilized UDP, CPC, MRB and NOM composites were studied in a similar way. In order to avoid repetition, in this subsection, a direct comparison is given between the respective systems reinforced by either PA6 or PA12 to help a better assessment of the reinforcing capability of the two polyamides.

Figure 14.10 compares the longitudinal Young's moduli E_1 obtained *in tensile mode* of all composite types under investigation. Generally, all UDP MFCs are better than the MRB and NOM composites. All UDP compositions (Figure 14.10a) are stiffer than the matrix. Both PA6 and PA12 UDP show a decrease of the Young's moduli when the YP concentration increases. As a whole, the stiffness of the PA6 and PA12 reinforced composites are quite similar. This is not the case with the MRB composites (Figure 14.10b), where the PA12 reinforcement performs better. They have higher Young's moduli than HDPE and the respective PA6 compositions. The PA6 reinforced composites are as stiff as the matrix or even worse as in the case of 65/30/5 system.

As seen in Figure 14.10c, the NOM composites displayed the lowest E_1 moduli. This was to be expected, having in mind the lack of orientation of the reinforcing constituent.

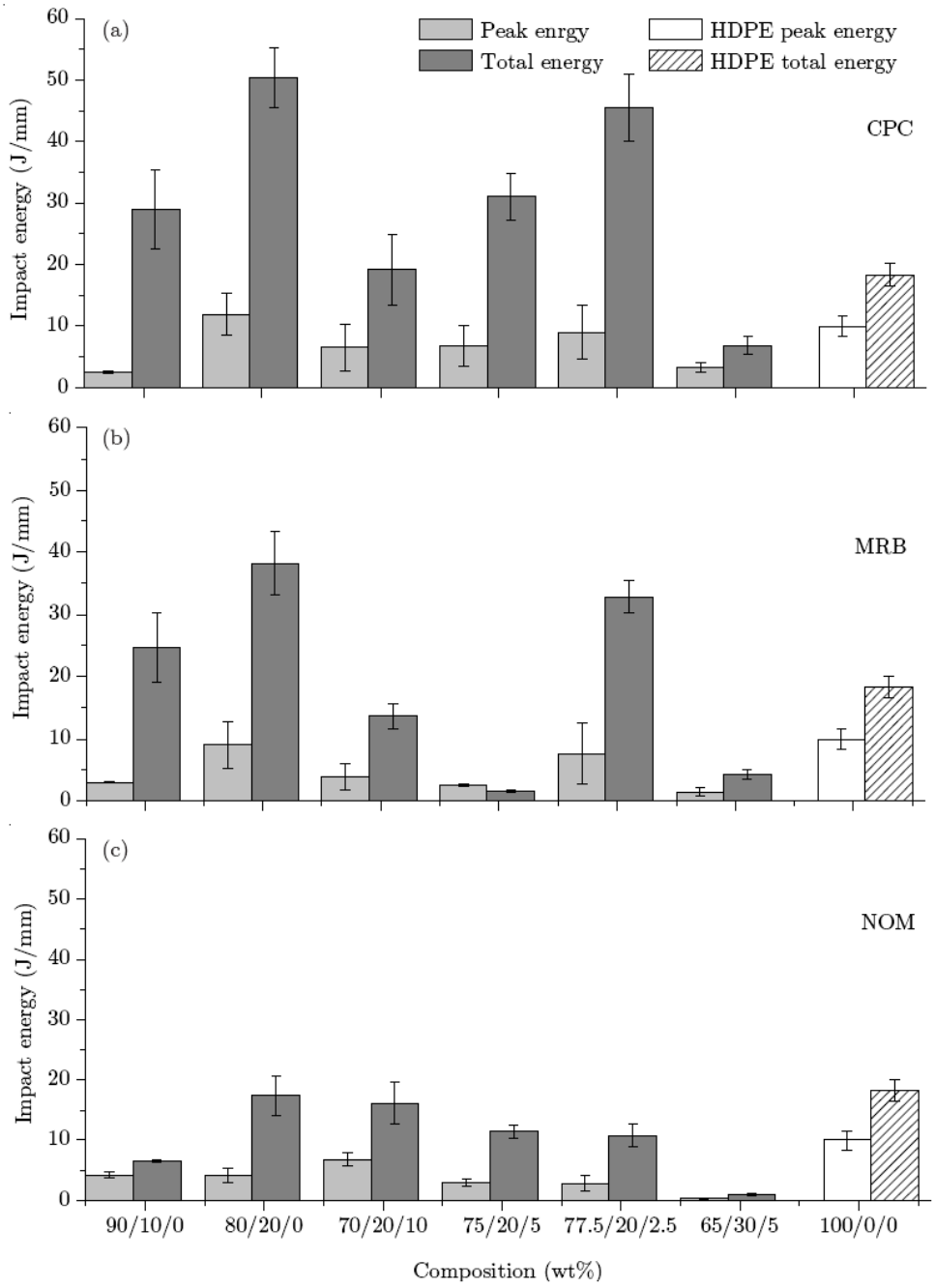

Figure 14.9. Impact energy/mm of HDPE/PA6/YP composites with various compositions and reinforcement: (a) cross-ply laminate MFC (CPC), (b) MFC with middle-length randomly distributed bristles (MRB), and (c) Composite prepared by non-oriented mixtures (NOM) [69]

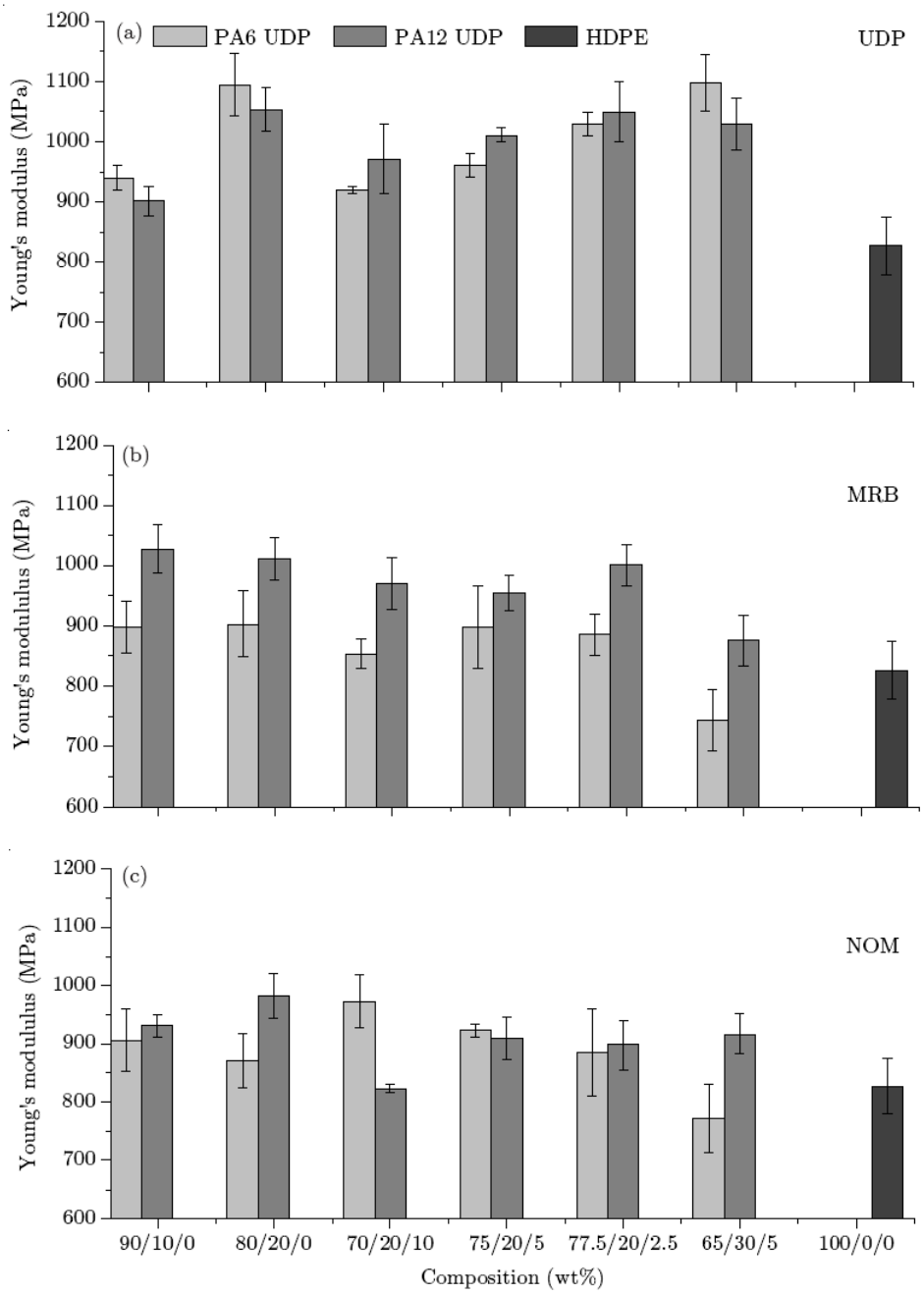

Figure 14. 10. Comparative charts of the Young's moduli of HDPE/PA6/YP and HDPE/PA12/YP composites: (a) CPC MFC, (b) MRB MFC, and (c) NOM composites

Two compositions are worth of special attention – the 80/20/0 and 70/20/10 where the influence of the two polyamides is completely different. The positive effect of PA12 is observed in the absence of compatibilizer, whereas the reinforcing action of PA6 is more effective at the highest YP concentrations. This difference is most probably caused by reasons related to the chemical composition.

Considering the tensile properties in general, another question about the influence of the chemical and physical structure arises. Based on the structure-properties investigations of the two polyamides in oriented state [73,78], it would be expected to have a better performance of all PA6-reinforced composites, which was not confirmed in the experiments. The possible explanation will be looked for in the next subsection.

The three-point flexural test is perhaps the only one where both PA6- and PA12 composites undoubtedly showed better performance in all compositions under investigation in the form of CPC, MRB and NOM (Figure 14.11). Irrespective of the orientation and alignment of the reinforcing constituent, all samples display notably better flexural stiffnesses, *CR*, as compared to the HDPE, even with the lowest polyamide content. Although there is no big difference in the flexural behavior of the CPC, MRB and NOM composites, those with oriented polyamide component, either PA6 or PA12, perform better. As a whole, the PA12 containing composites showed better flexural behavior, keeping higher *CR* values in all systems studied. The improvement varies in the range of 60–180% for the PA12 laminates and between 50 and 90% for the PA6 laminates. From all compositions the best performing composite was based on PA12 65/30/5 CPC that displays a *CR* of 4.2 GPa, which is 2.8 times higher than the respective HDPE value.

Figure 14.12 compares the data from the impact tests: the peak and the total impact energies per unit thickness of PA6- and PA12 CPC, MRB and NOM composites. The data are quite heterogeneous and do not suggest clear trends. Nevertheless, as regards the CPC systems (Figure 14.12a), PA12 reinforcement leads to improvement of the peak energy values, which are higher than the HDPE and the respective PA6 compositions. This means that the PA12 reinforcement in the CPC laminates works better as far as the peak energy is concerned. However, in respect to the total energy (Figure 14.12b) the comparison with PA6 is not so clearly in favor of PA12. The PA6 systems without (80/20/0) or with low YP concentrations (77.5/20/2.5) are better than the equivalent PA12 reinforced composites. The same considerations are valid also for the MRB composites with PA6 and PA12 (Figure 14.12c and d) although the peak and total energies here are lower than the respective CPC composites. In most of the MRB compositions the two energies are close or lower than HDPE matrix. The absence of orientation of the reinforcing component (Figure 14.12e and f) leads to a considerable decline of the toughness in both PA6 and PA12 NOM systems. A clear indication of these experiments is that the full potential of the PA6 and PA12-MFCs in impact is only

reached when the material is used in the form of laminates with proper ply alignment.

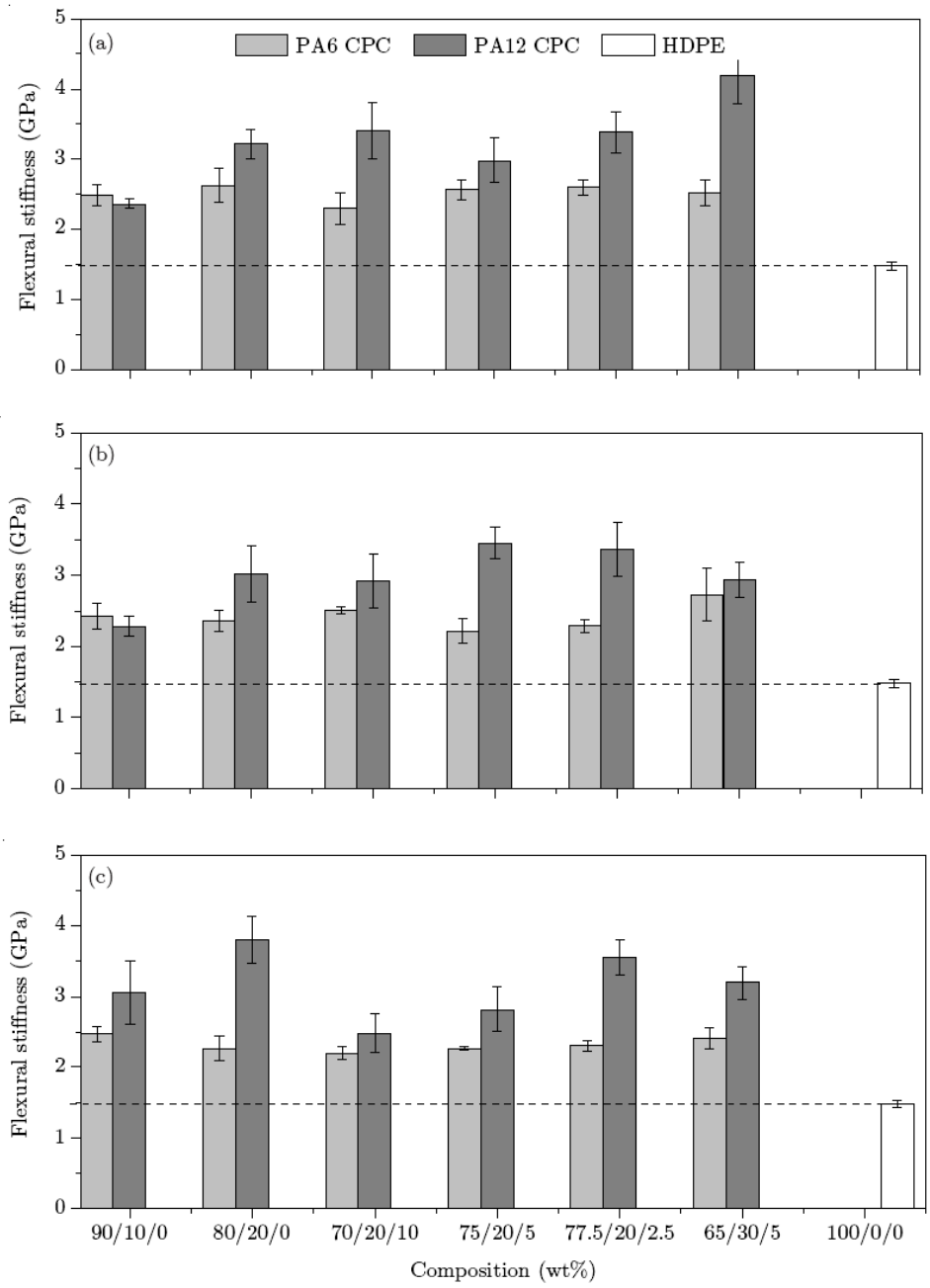

Figure 14.11. Comparative charts of the flexural stiffness of HDPE/PA6/YP and HDPE/PA12/YP composites: (a) CPC MFC, (b) MRB MFC, and (c) NOM composites

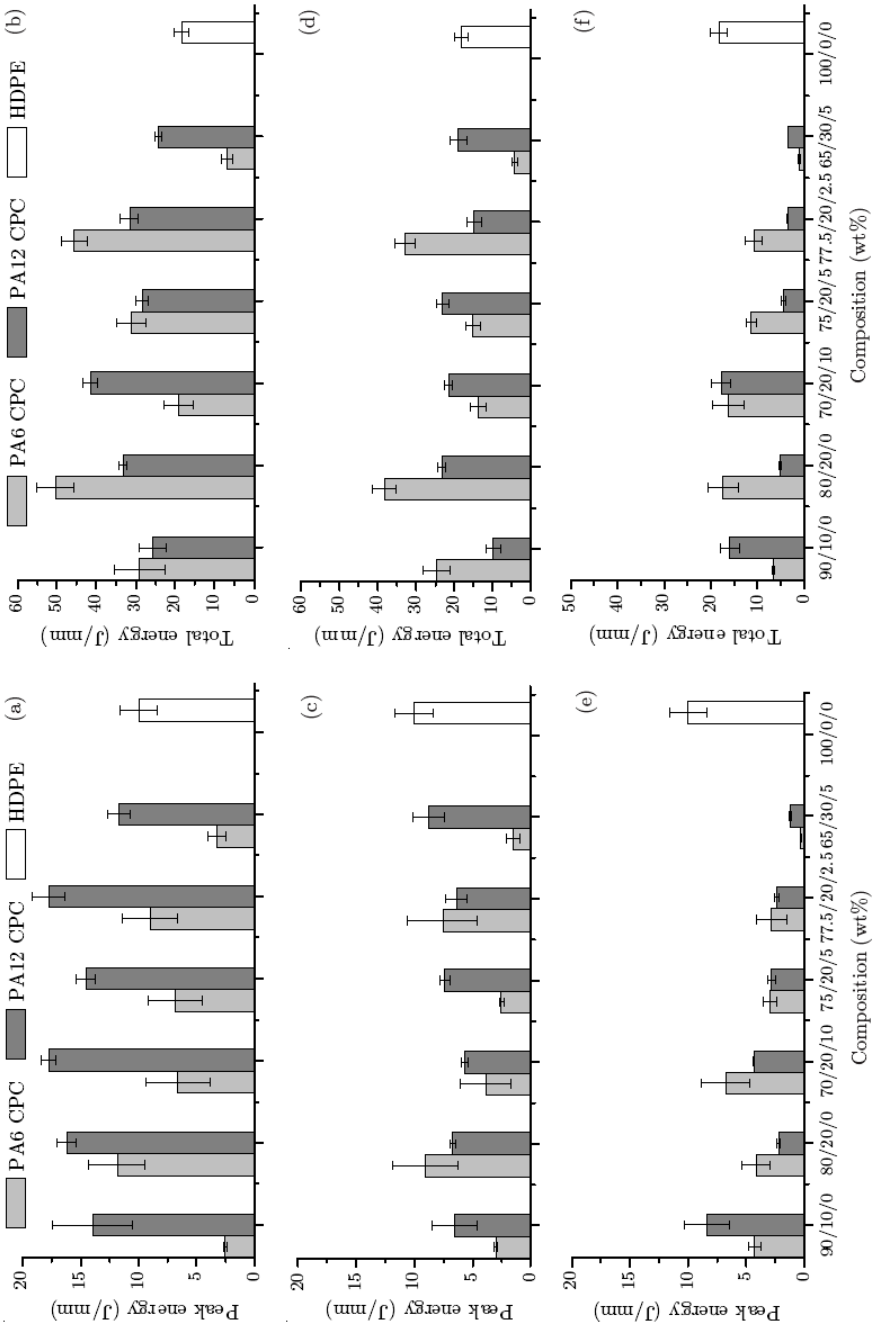

Figure .12. Comparative Impact test of HDPE/PA6/YP and HDPE/PA12/YP composites: (a), (b) Peak and Total energies of CPC MFCs; (c), (d) Peak and Total energies of MRB MFCs; and (e), (f) Peak and Total energies of NOM composites

14.4. Structure-properties relation in microfibrillar composites

Summarizing the results from the mechanical characterization of the HDPE/PA6/YP and HDPE/PA12/YP composites, it can be concluded that the improvement of the Young's moduli of the anisotropic UDP MFCs reinforced by unidirectionally aligned fibrils were in the range of 30% for both PA6 and PA12, while the tensile strength grew with 120% (PA6) and 150% (PA12) in respect to the HDPE matrix. The tensile properties of the UDP composites in transverse direction were close to or slightly higher than HDPE. As a rule, all anisotropic composites with the biggest concentration of compatibilizer YP showed the smallest enhancement of the tensile properties. Analogously, the best flexural stiffness was achieved in the absence of or at low concentration of YP, the improvement factor IF being of 75–80% for best PA6-reinforced CPC composites, reaching 130% for PA12 reinforcement.

Interestingly, a better mechanical performance of the PA12 reinforced composites was observed, which was quite unexpected having in mind that some of the mechanical properties of PA6 (*i.e*., tensile and impact strengths) are reportedly higher than those of PA12 [79,80]. The absence of fibrillar morphology of the reinforcing component (*i.e.*, no MFC structure present) or improper amount of compatibilizer led to poor mechanical properties of the final composite. Therefore, the explanation of the reinforcing effect should be related in the first place with proving and characterizing the fibrillar morphology of the MFCs and determining the AR of the PA fibrils. This is normally done by electron microscopy methods: SEM and transmission electron microscopy (TEM). On the other hand, the last step of the MFC's production cycle involves non-isothermal crystallization of the selectively molten matrix in the presence of the oriented and crystalline PA fibrils with diameters from several hundred nanometers to several micrometers. It is well-known that under such thermal conditions heterogeneous nucleation can occur with sufficiently high density along the interphase region leading to the formation of layers of matrix material around the fiber, known as *transcrystallinity* (TC) or *transcrystalline layers* (TCL) [81]. This phenomenon should also be investigated in relation to mechanical performance.

The first extensive SEM investigation of PA6/PET-based MFCs and their precursors performed by Evstatiev *et al.* [82] undoubtedly showed the fibrillar structure of the PET reinforcements preserved after the PA6 matrix isotropization. Since then, electron microscopy has been used to visualize the orientation and morphology of the matrix and reinforcing components in almost every report on MFCs. It is worth noting some more recent studies on MFCs comprising LDPE and PET as matrix and reinforcement, respectively [30,31]. Several microscopic techniques were used, *e.g*., SEM, polarizing light microscopy (PLM) and TEM. Thus, by SEM it was demonstrated that the isotropic LDPE matrix embedded PET microfibrils with random orientation. PLM and TEM of thin slices showed the

orientation in the machine direction. The latter method revealed also the formation of transcrystalline layers of LDPE on the oriented PET microfibrils.

Similar investigations were performed by Li *et al.* [43] by means of SEM and atomic force microscopy (AFM). The authors visualized the transcrystalline morphology of PP/PET MFCs proposing a shish-kebab model. MFCs containing blends of polycarbonate (PC) and HDPE were also produced and characterized by SEM, thus proving the presence of PC fibrils in the polyolefin matrix [83]. Our own SEM and PLM results demonstrated the morphology changes along the extruder line during the melt blending and fibrillation stages of a HDPE/PA12 blend (80:20 wt%) [61].

As regards the studies on transcrystallinity in conventional fiber reinforced composites, their number is vast. A number of issues are related to the formation and growth of TCL [81]: crystallinity of the matrix, mismatch of thermal coefficients of the fiber and the matrix, epitaxy between the fiber and the matrix, surface toughness, thermal conductivity, treatment of fiber, *etc*. Processing conditions such as cooling rate, temperature, and interfacial stress were also found to be important. There are indications that the TC phenomenon is probably too specific for each fiber/matrix system. Nevertheless, it has been recognized that the orientation distribution of the polymer chains in the TCL will determine the nature and extent of its effect on the mechanical properties of the composite material [84].

There exist a limited number of studies on the occurrence of transcrystallinity in MFC. Li *et al.* [38,42,43] studied the crystal morphology of iPP/PET *in situ* MFC, prepared by a slit extrusion – hot stretching-quenching process, and found that transcrystallinity occurred around the PET *in situ* microfibrils. The authors propose different nucleation mech26 Z. Denchev, N. Dencheva anisms related to the external field applied to explain this form of crystallization. MFC obtained *in situ* from LDPE matrix reinforced by PET microfibrils (LDPE /PET=1:1) [31] were injection molded and the formation of transcrystalline layers of LDPE matrix on the surface of the PET microfibrils was observed by TEM. In these layers the crystalline lamellae were aligned parallel to each other and were placed perpendicularly to the fibril surfaces. An interesting observation was made in PA12/PET MFC [85,86]. The PET microfibrils were not only effective nuclei for the PA12 macromolecules, but also caused their reorientation by 90º with respect to their initial direction: from parallel to the main chain direction of PET macromolecules in the oriented precursor to perpendicular in the MFCs.

It can be concluded that although transcrystallization was observed in some MFC systems, as yet this phenomenon is far from being completely understood. As MFC belong to the fiber reinforced composites, their mechanical properties will be expected to depend, just like the conventional fiber composites, on the effectiveness of the transfer of stress between the fiber and matrix [87], *i.e*., on the structure and geometry of the TCL.

In this chapter a combination of SEM and synchrotron X-ray scattering techniques is presented as a way to investigate the development of morphology and nanostructure in a series of HDPE/PA oriented blends with different composition during their processing to MFC with unidirectional orientation of the reinforcing fibrils. Transcrystallinity of HDPE is studied and an estimation of the TCL thickness is made. Models are proposed explaining the structural and mechanical data of PA-reinforced MFCs. In doing so, structural information about oriented and isotropic neat PA6 and PA12 was used, which was obtained previously under conditions similar to those of the MFC preparation [72,73,78].

14.4.1. *Microscopy studies of HDPE/PA6 and HDPE/PA12 systems*

Figure 14.13 displays selected SEM images of PA6-containing composite materials at different stages of the MFC processing: the MFCs after the extruder die (column 1), the MFCs after the first haul-off unit (column 2), and the final MFCs in the form of UDP (column 3). To observe the reinforcing fibrils, the specimens were cut in such a way that the fracture plane was parallel to the fibril axis. Figure 14.13, image 6c, presents the MFC containing the maximum amount of PA6. This sample was impossible to fracture like all the others. In this case the observation of fibrils by SEM was possible only after selective dissolution of the HDPE matrix in hot toluene for 5 h. Because of the removal of the matrix, the reinforcing fibrils lost their original parallel alignment in the composite.

As shown in Figure 14.13, in the samples without YP in Figure 14.13 1a, 2a, immediately after the extruder die, the PA6 component was well dispersed in globular domains (nodules) with average diameters of 3–4 μm. In the presence of YP (Figure 14.13,3a–5a), the diameter of the globules became significantly smaller (*ca.* 1.5 μm); that is, the higher the compatibilizer concentration, the smaller the PA6 nodules. Such a well-expressed reduction of the size of the dispersed component was observed earlier and recognized as an indication for the grafting of PA6 onto the MAH-containing compatibilizer [88]. An additional effect of the compatibilizer, evident from the SEM images, was the narrower size distribution of the reinforcing component within the HDPE matrix. In the system with 30% PA6 (Figure 14.13, 6a), the diameters of the PA6 droplets reached the highest value, about 4.5 μm. This may have been due to the unfavorable combination of a high PA6 concentration with a low amount of the compatibilizer, which prevented good mixing of the system.

As expected, after the first haul-off unit (Figure 14.2, 1b–6b), the diameter of the polyamide entities decreased up to 3.5 times because of their stretching.

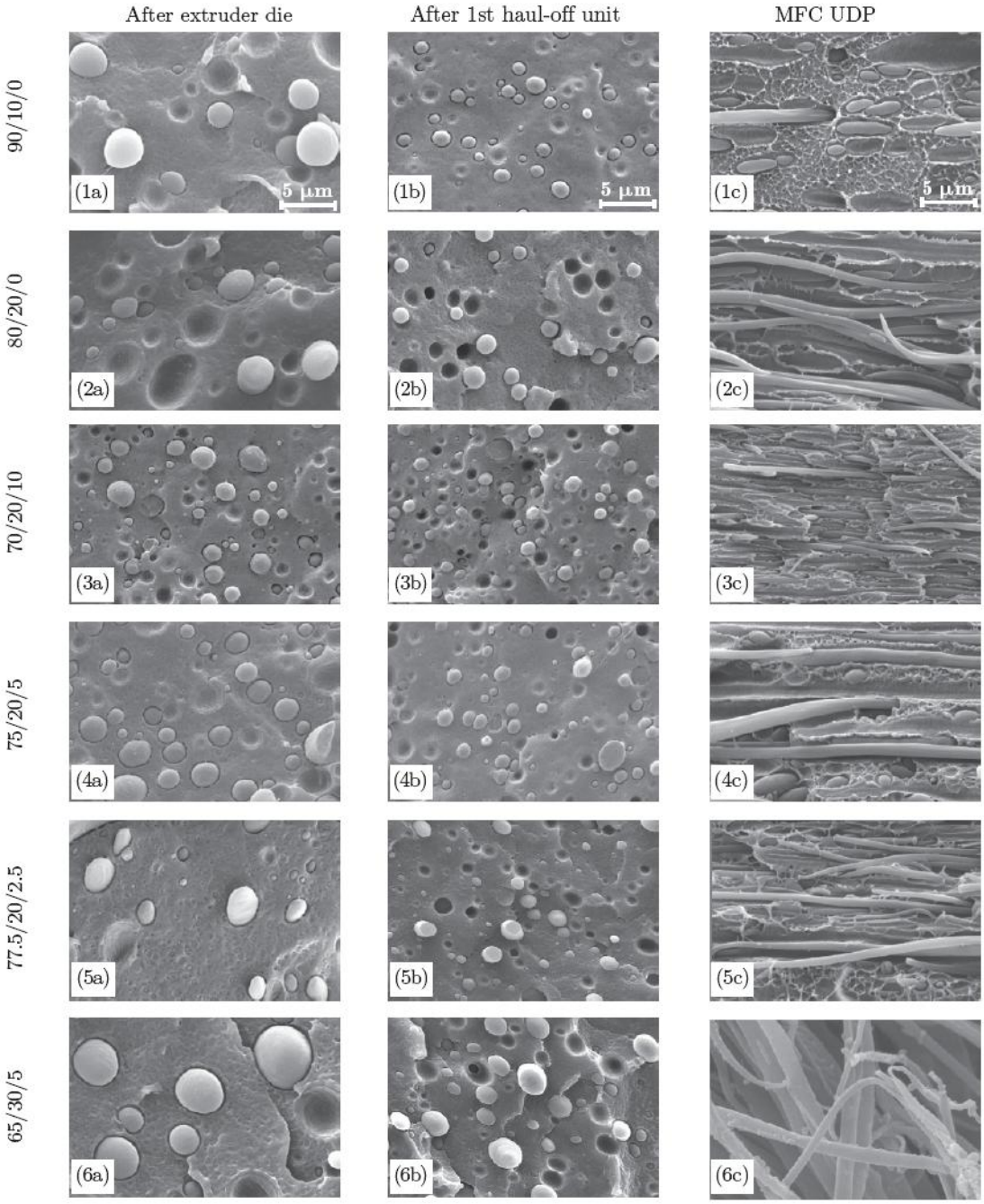

Figure 14.13. SEM images of HDPE/PA6/YP surfaces after cryogenic fracture at the various stages of the MFCs preparation (compositions given in wt%): non-oriented blend right after the extruder die (1a–6a); slightly oriented blends after the first haul-off unit (1b–6b); UDP composites fractured along the fibrils axis (1c–5c); UDP composite 65/30/5 after selective extraction of the HDPE matrix (6c) [63]. All the images are taken at the same magnification

The SEM images of the final MFCs (Figure 14.13, 1c–6c) deserve special attention. The SEM method undoubtedly confirmed that: (i) the PA6 reinforcing component had a well-expressed fibrillar morphology, and (ii) the average diameters of these fibrils were in the upper nanometer to lower micrometer range (*e.g.*, between 700 and 1000 nm).

None of the images of MFCs in Figure 14.13 permitted us to measure the fibril length directly. Indirectly, the average lengths and ARs of the reinforcing PA6 fibrils could be evaluated after some simplifying suppositions were made. The micrographs show that at the extruder die (*i.e.*, in the absence of orientation), the PA6 entities were globular (Figure 14.13, 1a–6a). After the diameters of these globules were measured, the average volume of the spherical PA6 entities could be calculated. Furthermore, the diameters of the fibrils in the final MFCs were measured from Figure 14.13, 1c–6c, and were averaged. Under the assumption that the fibril geometry was cylindrical and that the fibrils were produced by the deformation of the respective PA6 spherical nodules without the formation of voids (*i.e.*, the volumes of the PA6 spheres at the extruder die and of the MFC fibrils were the same), we could estimate the average length of the fibrils and therefore the AR (Table 14.6).

Table 14.6. Dimensions of the PA6 reinforcing phase in various HDPE/PA6/YP materials as revealed by SEM measurements [63]

Composition HDPE/PA6/YP, (wt%)	Diameters of PA6 nodules at ED, (nm)	Dimensions of the PA6 fibrils after the 1st haul-off unit			Dimensions of the PA6 fibrils in UDP MFC		
		Average diameter, (nm)	Estimated length, (nm)	Max. aspect ratio	Average diameter, (nm)	Estimated length, (nm)	Max. aspect ratio
90/10/0	3500	1200	19850	16.5	1000	28600	28.6
80/20/0	3500	1000	28600	28.6	750 (570)	50815 (87668)	67.8 (153.5)
70/20/10	1500	500	9000	18	700 (714)	4592 (4414)	6.6 (6.2)
75/20/5	2000	1250	3413	2.7	800	8333	10.4
77.5/20/2.5	2750	1250	8873	7.1	750	24650	33.0
65/30/5	4500	1500	27000	18	1000	60750	60.8

Notes: ED = extruder die; The values in parentheses are for oriented blends after the selective extraction of the HDPE matrix; The estimations of the microfibrils lengths are made supposing that one PA6 globule at ED produces one microfibril in the final UDP MFC. The role of coalescence for microfibril formation in the HDPE/PA blends is considered further in the text.

Thus, in non-compatibilized PA6-reinforced MFCs, the calculated length of the reinforcing fibrils was up to 51 μm, whereas the maximum length in the MFCs containing 20% PA6 in the presence of the compatibilizer was 5–25 μm. Keeping in mind the variation of the fibril diameters, we could estimate the AR (Table 14.6).

It can be seen that the non-compatibilized 80/20/0 sample and the sample with 30% PA6 showed the highest maximum ARs, which went down gradually as the YP content was increased.

Figure 14.14 shows micrographs of the composites produced from different precursors. The influence of the alignment of the reinforcing phase on the morphology could be seen in two representative MFCs: one without the compatibilizer (80/20/0) and one with 10 wt% of compatibilizer (70/20/10).

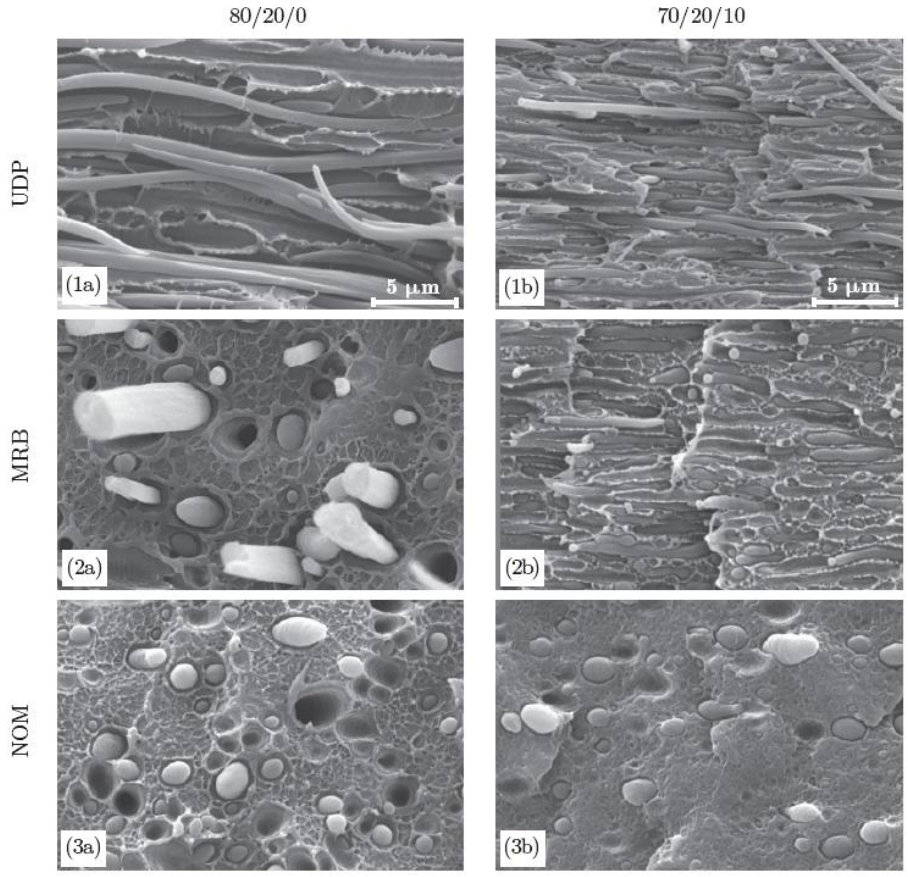

Figure 14. 14. SEM images of surfaces (after cryogenic fracturing) of MFCs made from two HDPE/PA6/YP blends [1a–3a: 80/20/0 wt%; 1b–3b: 70/20/10 wt%]: UDP – unidirectional ply fractured parallel to the fibril direction; MRB – composite from middle-length PA6 bristles with random distribution; NOM – material obtained from non-oriented granules of the two blends [63]. All SEM images are taken at the same magnification

In UDPs, all the fibrils lay nearly parallel to the fracture plane (Figure 14.14, 1a,b). Figure 14.14, images 2a and 2b, presents composites produced from MRBs. There, a great variety of fibril cross-section shapes can be seen (rectangular, circular, or oval), depending on the angle between the fibril and the fracture plane. In the NOM

samples (Figure 14.14, 3a,b), however, only oval-shaped entities instead of fibrils were observed, and this indicated that after the extruder die, the orientation of the PA6 component was either absent or very low.

The images of Figure 14.14 display the improvement in the adhesion between PA6 and HDPE in the presence of compatibilizer. This effect is particularly clear when images 1a and 1b are compared. In the absence of YP (image 1a), the fibrils were completely detached from the matrix, whereas in the specimen with the compatibilizer (image 1b), they were well embedded, evidencing good adhesion.

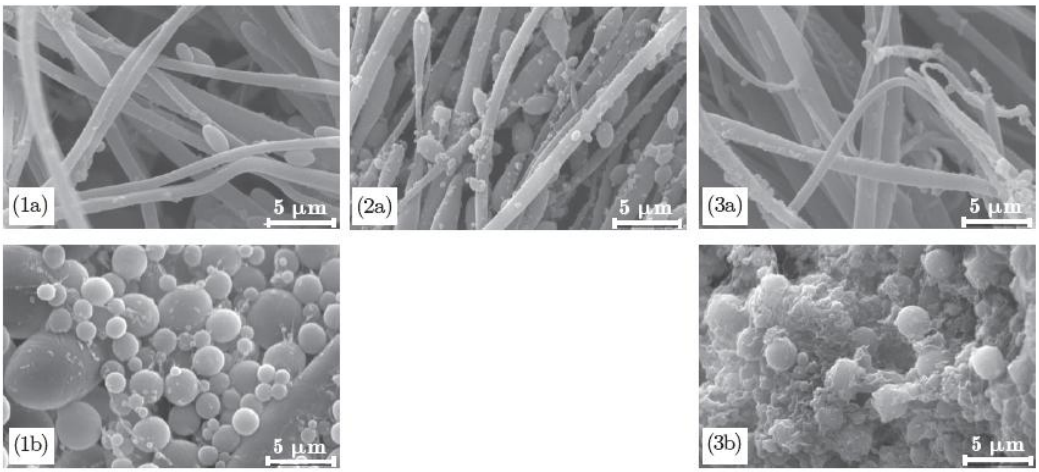

Figure 14.15. SEM images of HDPE/PA6/YP samples (after extraction of the matrix) with the following compositions (wt%): 1 – 80/20/0, 2 – 70/20/10, 3 – 65/30/5; (a) final MFCs, and (b) NOM after the die exit [63]

As previously confirmed [88,89], the copolymer formed between the PA6 fibril material and the MAH linkages of YP acted like a bridge between the HDPE matrix and the reinforcing PA6, thus strengthening the interface. It was interesting to check how the fibrils looked after the selective removal of the HDPE matrix material in the MFCs prepared without YP (Figure 14.15, 1a) and with YP at a 10 or 5% concentration (Figure 14.15, 2a, 3a). The extraction was performed with hot toluene, and the duration was kept the same for all the samples. Apparently, in the absence of the compatibilizer (Figure 14.15, 1a), the HDPE matrix was easier to dissolve and remove, the remaining fibrils being quite smooth. In the presence of 10% YP and after extraction, the fibrils were still covered by many globular fragments, most likely originating from the isotropic matrix. Increasing the PA6 content up to 30% and decreasing the percentage of YP (Figure 14.15, 3a) produced smooth fibrils similar to those when no compatibilizer was applied. It can be supposed that the fibril roughness in Figure 14.14 is related to the HDPE–PA6

copolymer, which is expected to be less soluble in toluene because of the inclusion of PA6 segments.

Figure 14.15 also shows that after the die exit (Figure 14.15, 1b, 3b), the reinforcing component was globular, and the linkage at the PA6/HDPE interface appeared to be stronger in comparison with the fibril reinforcements (Figure 14.15, 1a–3a). The fibril thicknesses in the latter images were quite similar, regardless of the sample composition.

Another interesting deduction can be made from the consideration of Table 14.6 and Figure 14.15. With the 80/20/0 sample, the selective extraction of the HDPE matrix material showed a drastic increase in AR (from *ca*. 68 to 154), whereas in the 70/20/10 sample containing the maximum amount of YP, the AR remained unchanged. This was an indirect indication that the reinforcing fibrils observed by SEM most likely contained a core of PA6 and a shell of HDPE, the latter being chemically bonded to the core in the MFCs containing YP or only physically attached to it in the non-compatibilized samples.

Using the same methodology, the HDPE/PA12/YP samples were studied by SEM (Figure 14.16, Table 14.7). The fibrils' orientation and morphology could be observed in the final MFC after fracturing the specimens in a direction parallel to the fibrils (Figure 14.16, samples 1c–6c, and Table 14.7).

Table 14. 7. Dimensions of the PA12 reinforcing constituent in various HDPE/PA12/YP materials as revealed by the SEM measurements. The values in brackets are observed after selective extraction of the HDPE matrix [64]

Composition HDPE/PA6/YP, (wt%)	Diameters of PA12 nodules at ED, (nm)	Dimensions of the PA12 fibrils after the 1st haul-off unit			Dimensions of the PA12 fibrils in UDP MFC		
		Average diameter, (nm)	Average length, (nm)	Average aspect ratio	Average diameter, (nm)	Average length, (nm)	Average aspect ratio
90/10/0	2500	1500	4630	3.1	500	41700	83
80/20/0	3125	2200	4200	1.9	625 (525)	52100 (52100)	83 (99)
70/20/10	2500	1500	4630	3.1	560 (450)	33216 (33216)	59 (74)
75/20/5	1875	1000	4395	4.4	625	11250	18
77.5/20/2.5	2500	1000	10417	10.4	750	18518	25
65/30/5	5000	1500	37037	24.7	1250 (900)	53333 (53333)	43 (59)

The fibril thicknesses depend on the YP and PA content and vary in a broad range between 0.5 and 1.5 μm. The finest fibrils are observed in the 90/10/0 sample and in the 70/20/10 MFC, the latter containing the biggest amount of compatibilizer (images 1c and 3c). The micrographs of the YP containing samples show clearly the above-mentioned improved adhesion in the presence of compatibilizer. The

fibrils look like being "cemented" into the HDPE matrix, which is not the case in images 1c and 2c where the fibrils are smoother and are, apparently, separated from the matrix.

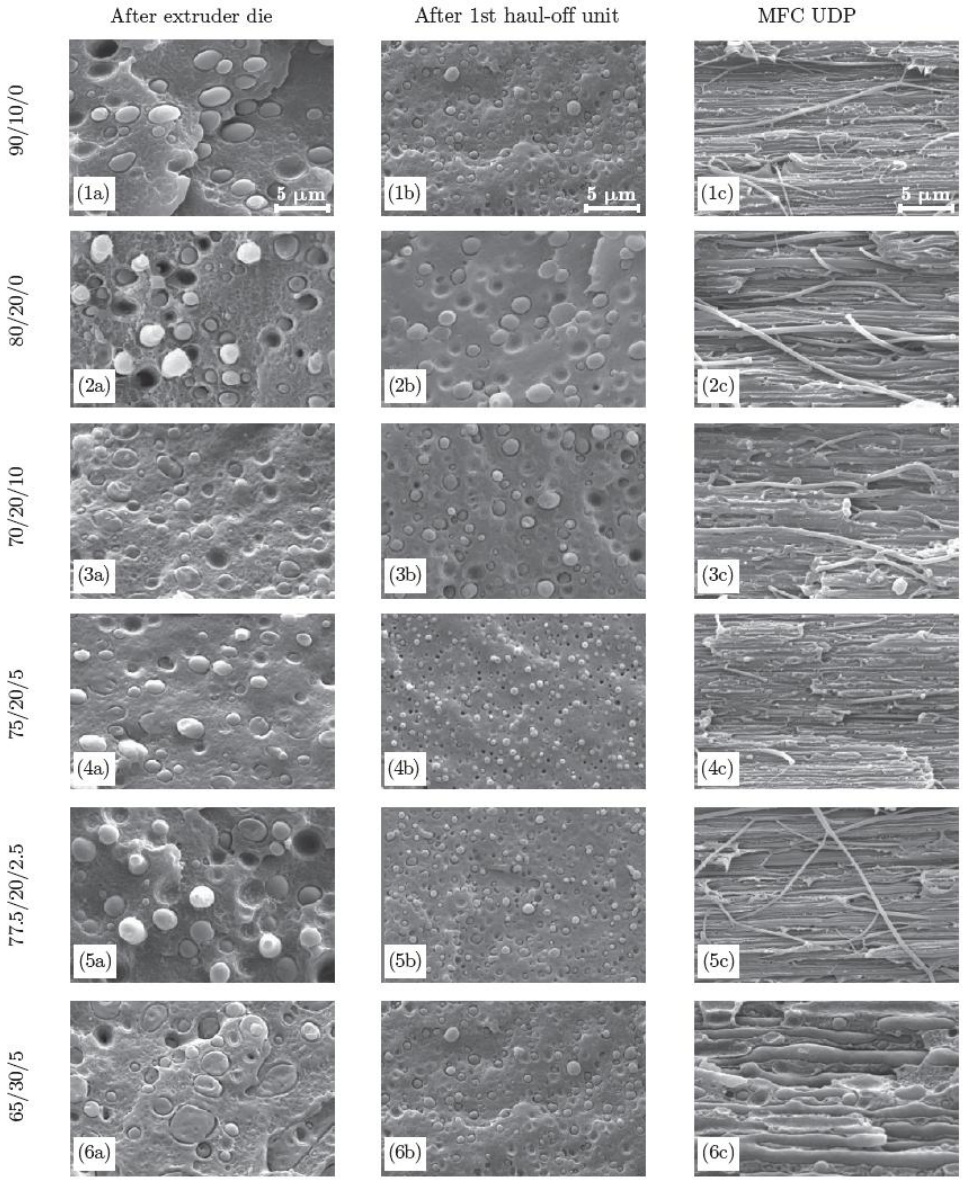

Figure 14.16. SEM images of cryogenic fractured surfaces of various HDPE/PA12/YP materials (compositions given in wt%) during the stages of the MFCs preparation: non-oriented blend after the extruder die (1a–6a); slightly oriented blends after the first haul-off unit (1b–6b); MFC UDP, fractured in the direction of the fiber (1c–6c) [64]. All the images are taken at the same magnification

The influence of compatibilizer on the PA12 composite morphology is further revealed in Figure 14.17. As with the HDPE/PA6/YP samples, the SEM images here were obtained after selective extraction of the HDPE matrix with hot toluene for 5 h. The PA12 reinforcing fibrils are with average diameters of 525 nm (no compatibilization – Figure 14.17, 1a, Table 14.7) and 450 nm for the sample with the largest concentration of compatibilizer (image 2a). Interestingly, the selective dissolution seems to remove the same amount of matrix material (*ca*. 18%) from the HDPE/PA12 composites with and without compatibilizer. This was not the case with the HDPE/PA6 MFC, where the 70/20/10 sample showed the same fibril thickness and AR before and after dissolution (Table 14.6). To explain this difference, one should consider the studies on the chemical reaction between polyeth ylene/MAH copolymers and the NH groups from polyamides [88] suggesting chain scission and formation of imide linkages, thus creating chemical bonds at the polyolefin/polyamide interface. Therefore, since PA12 contains only the half of the NH groups of PA6, the number of the effective imide linkages will be reduced causing weaker attachment at the interface.

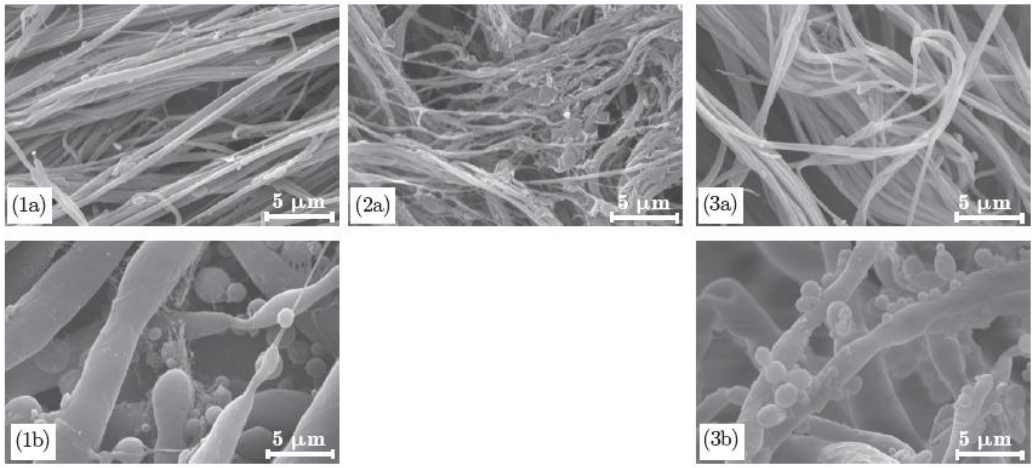

Figure 14..17. SEM images of various HDPE/PA12/YP samples after selective extraction of the matrix (a – final MFCs, and b – non-oriented blends after the die exit) with the following compositions (wt%): 1 – 80/20/0; 2 – 70/20/10; 3 – 65/30/5 [64]

Figure 14.18 shows the TEM micrograph of the 77.5/20/2.5 oriented cable. The PA12 reinforcing constituent is well distributed within the HDPE matrix. The PA12 fibrils' diameters vary in the 100–400 nm range, *i.e.*, in the oriented precursor blends they are significantly thinner than those in the final MFC (*ca*. 750 nm). Once again this fact can be explained with the formation of a TCL layer of HDPE upon the PA12 fibril during the compression molding stage when the final MFC is obtained.

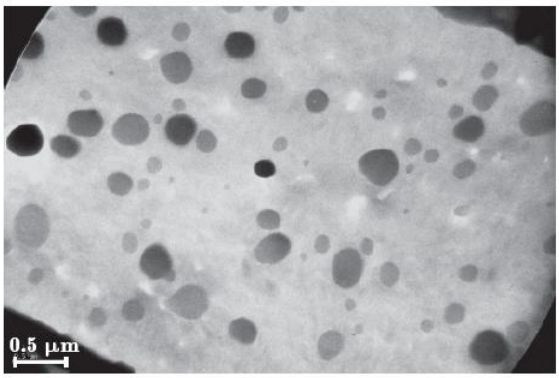

Figure 14. 18. TEM image of 77.5/20/2.5 HDPE/PA12/YP oriented precursor obtained after the second haul-off unit [64]

As in the case of HDPE/PA6/YP MFC, it can be supposed that the reinforcing fibrils in the PA12-containing MFCs most probably contain a core of PA12 and a shell of transcrystalline HDPE. Thus, on the basis of the electron microscopy experiments, the following model can be suggested visualizing the structural changes during the MFC preparation (Figure 14.19). According to the model proposed, right after the extruder die, the PA globules are embedded into an isotropic HDPE matrix. During the cold drawing stage, *i.e.*, in the oriented precursor cables, both HDPE and PA12 are fibrillated. During the compression molding at 160ºC, the HDPE fibrils melt and upon the subsequent cooling and crystallization of the matrix, the PA fibrils are coated with a TCL of HDPE material.

The model in Figure 14.19 suggests that each fibril is produced by elongation of one single polyamide globule. As shown by Fakirov *et al.* [90], the fibril formation in MFC precursors produced by drawing of PP/PET blends with compositions close to 50/50 wt% should be rather attributed to coalescence of PET globules and not to their deformation. In our case, however, the content of the fibril-forming PA component in the MFC studied is lower, in the 10–30 wt% range, which makes coalescence significantly less probable, especially in the samples with 10 and 20% of PA. Moreover, one has to keep in mind that the cold drawing in the HDPE/PA/YP MFC preparation was performed at 90–95ºC, *i.e.*, far below the melting point of both PA6 and PA12. At such low temperatures the coalescence process will be additionally hindered because of the poor diffusion conditions as compared to the case of molten polymers [91].

There are also other experimental observations in the HDPE/PA systems related to the number of the PA6 reinforcing fibrils, their crystallinity and the molecular orientation in them, as well as in the HDPE transcrytstalline layer thereupon that clearly contradict the coalescence model reasoning in [90] and are in favor of the model in Fig. 14.19.

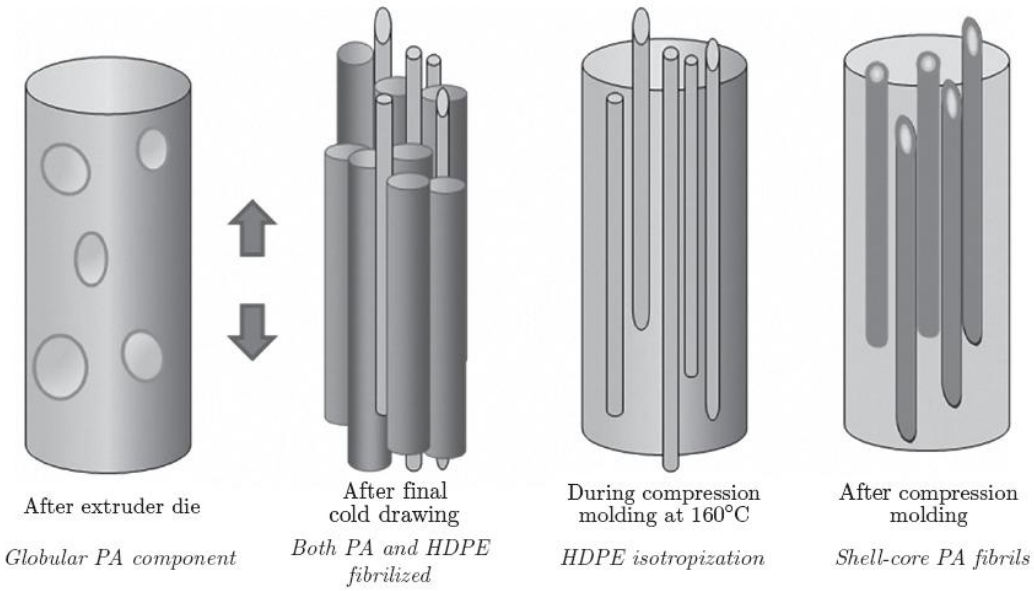

Figure 14. 19. Simplified model of the structural changes occurring at different stages of the MFC preparation [64]

The average lengths and ARs of the reinforcing PA12 fibrils can be estimated on the basis of the model in Figure 14 .19. Using the same suppositions as for the HDPE/PA6/YP MFCs, in non-compatibilized PA12-reinforced MFC the calculated lengths of the reinforcing fibrils are in the range between 42 and 52 μm, and with YP (20% PA12) – from 11 to *ca*. 33 μm. Again, the two non-compatibilized samples showed the highest maximum AR values being larger than 80 that fluctuated with the YP content. In fact, having in mind the decrease of the fibrils' diameters after selective extraction, the real AR values (*i.e*., after leaving out the HDPE TCL) should be even larger. A possible way to verify the real AR is to obtain an estimate of the TCL thickness by other methods such as X-ray scattering.

14.4.2. *Synchrotron X-ray studies of HDPE/PA6 and HDPE/PA12 MFC*

Wide- and small-angle X-ray scattering (WAXS, SAXS) are frequently employed for structural investigations of transcrystallinity in conventional and nanostructured fiber composites. Thus, Feldman *et al.* [92] studied the structural details of PA66 transcrystallinity induced by the presence of aramid (Kevlar 29, 49 and 149) and carbon (pitch based) fibers, as determined by high resolution synchrotron WAXS. The main observation was that the orientation was distinct for each system and almost independent of distance from the fiber. In an earlier X-ray diffraction study of aramid and carbon fiber-reinforced PA66, it was concluded that in the nucleation and initial growth stages the first chain folds were oriented so that the chain axis was aligned in the fiber direction, and in the crystal growth that followed a typical

sheaf structure was formed (described graphically in [93]), leading gradually to spherulite formation, as in bulk crystallization [94]. WAXS analysis performed on PE fiber- reinforced HDPE matrix [95,96] revealed that TC layer was grown on the fiber surface originating from matrix material with properties depending on the processing conditions. A smooth and banded TC morphology developed under ice-water quenching and air cooling conditions, whereas under isothermal crystallization an apparent rod-like morphology was observed to develop in the matrix. Additional examples for TC investigation by X-ray techniques are pointed out in the excellent review of Quan *et al.* on transcrystallinity in polymer composites [81] revealing the state-of-the-art in the area until 2005.

More recently, polymer transcrystallinity induced by CNT in PP matrices was studied by Zhang *et al.* [97]. It was concluded that supramolecular microstructures of PP transcrystals induced by the nanotube fiber are observed in the range of isothermal crystallization temperatures from 118ºC to 132ºC. WAXS analyses have shown that the nanotubes can nucleate the growth of both α- and γ-transcrystals, whereby the α-transcrystals dominated the overall interfacial morphology. Also, close to the nanotube fiber surface, a cross-hatched lamellar microstructure composed of mother lamellae and daughter lamellae has been observed. As far as other advanced X-ray scattering studies in polymer composites are concerned, it is worth mentioning also the study of Hernández *et al.* [98]. The relationships between the macroscopic deformation behavior and microstructure of a neat poly(butylene terephthalate)-block-poly(tetramethylene oxide) (PBT-b-PTMO) block copolymer and a polymer nanocomposite (PBT-b-PTMO) containing 0.2 wt% single wall CNT were investigated by simultaneous synchrotron SAXS and WAXS during tensile deformation. The structural data allowed the conclusion that the CNT acted as anchors in the nanocomposite, sharing the applied stress with the PBT crystals and partially preventing the flexible, non-crystallizable PTMO chains to elongate.

This chapter reveals our recent synchrotron SAXS and WAXS studies on transcrystallinity in HDPE/PA/YP UDP composite materials [63,64]. In this specific case, both the matrix and the reinforcement are semicrystalline polymers with similar crystallographic characteristics. Unless otherwise specified, all WAXS and SAXS patterns in this study were registered at the soft condensed matter beamline (A2) of HASYLAB, Hamburg, Germany, using synchrotron radiation with a wavelength fixed to 0.15 nm. The sample-to-detector distance for SAXS was set at 2830 mm, the diffraction patterns being registered by means of a MAR CCD 2D detector. For the WAXS measurements the detector was positioned at 90 mm in respect to the sample. The various MFCs were studied in transmission mode, the exposure time being 10 s for WAXS and 30 s for the SAXS patterns. A sample holder allowing for controlled heating/cooling cycles in the 30–300ºC range was used.

14. 4.2.1. *Small-angle X-ray scattering*

Figure 14.20 presents SAXS patterns of two HDPE/PA6/YP UDP MFC samples: images 1 without the compatibilizer (80/20/0), and images 2 – with the compatibilizer (70/20/10) at different temperatures. The visual inspection of the initial 2D SAXS patterns at 30ºC (images 1a and 2a) showed that both composites contained isotropic scattering of randomly distributed lamellar structures and equatorial scattering maxima attributable to lamellar crystals oriented parallel to the horizontal fiber direction. The isotropic ring and the oriented maxima displayed similar long spacings greater than 220 Å. This was a clear indication that the observed oriented reflections could not have originated from the reinforcing PA6 component, whose long spacings are typically between 70 and 90 Å [72]. Consequently, it can be supposed that a fraction of the HDPE matrix material crystallized on the oriented PA6 fibrils, thus forming a TCL at the interface.

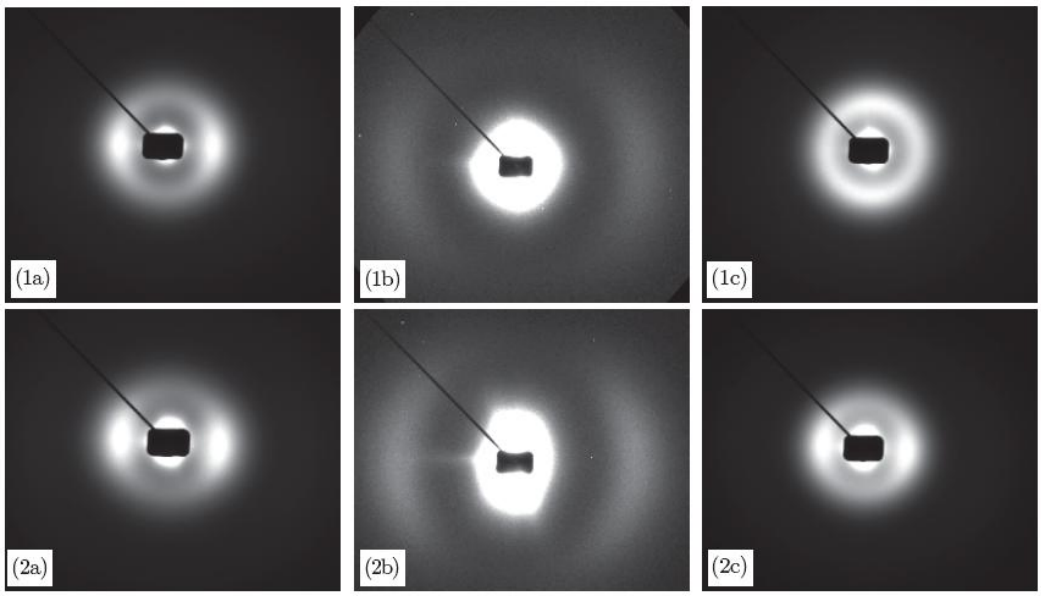

Figure 14.20. 2D SAXS images of two HDPE/PA6/YP UDP microfibrillar composites with compositions: 1 – 80/20/0; 2 – 70/20/10; at different temperatures: (a) pattern of starting MFC at 30°C; (b) pattern at 160°C, heated in the beam; (c) pattern at 30°C after heating at 160°C. The fibril axis is horizontal [63]

Without a special treatment of the patterns, it was impossible to observe at the same time the HDPE and PA6 scattering in Figure 14.20, 1a and 2a, because of the strong differences in the scattering intensities. Heating the two UDP MFC samples at 160ºC eliminated the HDPE scattering and revealed the oriented PA6 reflections (images 1b and 2b). Cooling to 30ºC caused the HDPE matrix to

recrystallize. This process took place differently in the two MFCs under investigation. The oriented HDPE TCL in the 70/20/10 MFC at 30ºC after the selective melting of the matrix maintained its equatorial orientation (Figure 14.20, 2c), whereas in the 80/20/0 system, it rotated by 90º and appeared at the meridian (Figure 14.20, 1c). Isotropic scattering was also present in these two patterns.

This reorientation of the HDPE scattering was better observed when azimuthal cuts of the aforementioned patterns were performed (Figure 14.21). The curve of the noncompatibilized sample (Figure 14.21a) clearly shows that after recrystallization, the peak of the intensity was not at 0º (*i.e.*, along the fiber axis) but was at –90 or 90º. In the compatibilized sample (Figure 14.21b), the azimuthal distribution of the scattered intensity remained the same at 30ºC and at 30ºC after 160ºC. It is noteworthy that this reorientation of the lamellae that took place in the non-compatibilized samples was not accompanied by chain direction reorientation; that is, the chain direction of PA6 and that of the oriented HDPE fraction continued to coincide, as in the starting image at 30ºC. This effect is discussed in the next subsection, which is dedicated to the WAXS studies.

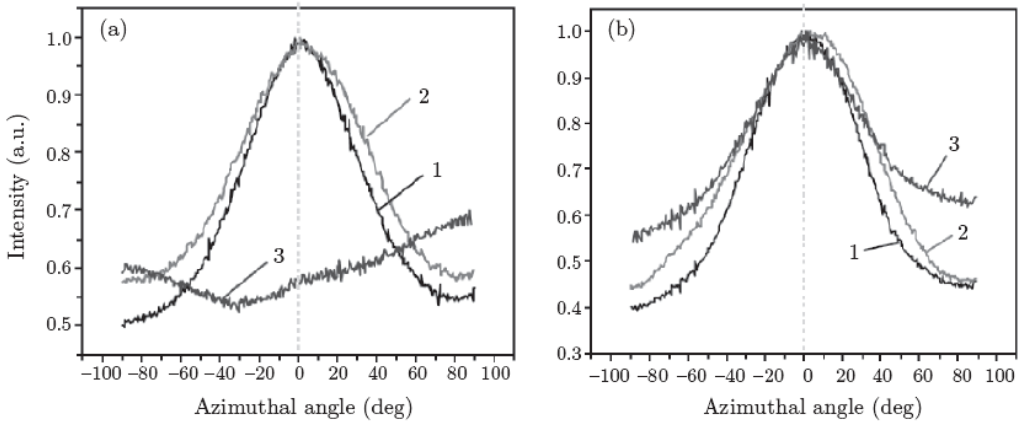

Figure 14.21. Azimuthal distribution of the scattered intensity in the 2D SAXS images of two HDPE/PA6/YP UDP MFCs with compositions of (a) 80/20/0 and (b) 70/20/10: (1) the initial MFC at 30ºC, (2) the MFC with in-beam heating at 160ºC, and (3) the MFC at 30ºC after heating to 160ºC. The dashed line indicates the fiber direction [63]

To make a distinction between the two fractions of HDPE, the subtraction procedure described by Nogales *et al.* [99] was used. The 2D SAXS patterns were first corrected for the incident beam intensity, and then the empty chamber scattering was subtracted. It was assumed that the total scattered intensity could be separated into two contributions: (i) the contribution of the amorphous chains being in the isotropic state and the non-oriented crystals, which was directly proportional to the azimuthally independent component of the total scattered intensity, and (ii) the oriented contribution from all oriented scatterers (with various degree of

orientation), which was calculated by subtraction of the azimuthally independent component from the total scattered intensity. To determine the azimuthally independent intensity and to perform the subtraction, a subroutine incorporated into Polar 2.7.1 X-ray software was used [100].

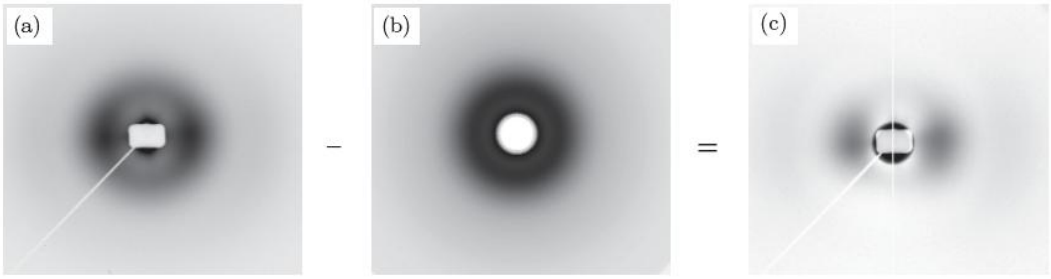

Figure 14.22. Deconvolution procedure of the SAXS pattern of the 75/20/5 UDP MFC. (a) original SAXS image; (b) intensity pattern of the isotropic scattering; (c) intensity pattern of the oriented scatterers obtained by subtraction (a) – (b) [12]. The fiber axis is horizontal [63]

Thus, Figure 14.22a shows the pattern of the total scattering of the 75/20/5 UDP MFC composition at 30ºC. The computer-generated 2D image of the isotropic intensity is presented in Figure 14.22b, and the resulting image (obtained after the subtraction of part b from part a) corresponding to the oriented scattering is shown in Figure 14.22c. As the latter shows, the procedure not only separated the two HDPE components but also revealed the oriented PA6 fraction located along the equator. In Figure 14.23, three-dimensional (3D) visualization of the initial pattern (Figure 14.23a) and the oriented scattering (Figure 14.23b) for the same 75/20/5 composition is presented.

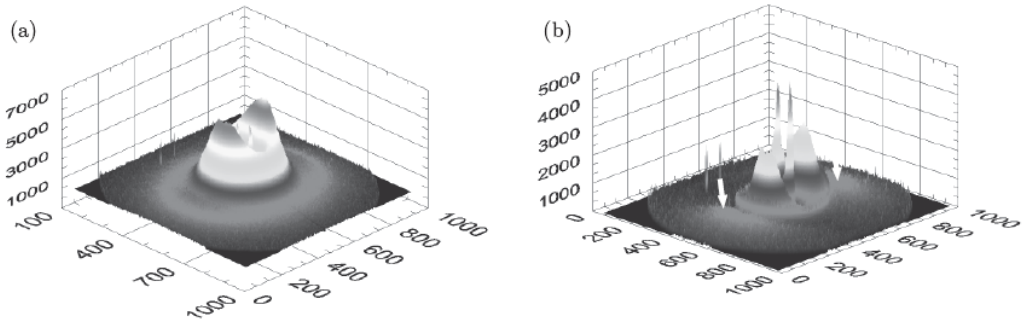

Figure 14.23. 3D SAXS patterns of 75/20/5 HDPE/PA6/YP UDP MFC before (left) and after (right) subtraction of the azimuthally independent component of the total scattered intensity. The white arrows indicate the scattering of the PA6 reinforcing component [63]

The latter shows better the PA6 contribution to the oriented part of the scattering, which is indicated by arrows, proving that the UDP MFC contains uniaxially oriented PA6 oriented fibrils.

Table 14.8 presents the HDPE and PA6 Bragg long-spacing values (*LB*) determined from the scattering patterns of six UDP MFCs with different HDPE/PA6/YP compositions. In the absence of the compatibilizer, there were no significant differences between the *LB* values of HDPE lamellae located in the bulk (isotropic) and those of the oriented HDPE lamellae in the TCL (oriented). Introducing YP resulted in smaller long periods in the oriented HDPE fraction, whereas those of the bulk matrix fraction remained like those in the non-compatibilized compositions. Only in the 65/30/5 UDP MFC the long spacings of the oriented HDPE lamellae was greater than that of the isotropic fraction. Most likely, this could be explained as a result of the larger amount of PA6 in this composition. With respect to the PA6 long-spacing values, they varied in the range of 77–95 Å. The PA6 *LB* of 77 Å in the 65/30/5 composition was the closest to the value of the oriented neat PA6 [72,73].

Table 14. 8. Long spacing values of the HDPE/PA6/YP UDP composites at 30°C without (L_B) and with (L_B^*) deconvolution [63]

No	HDPE/PA6/YP composition, (wt%)	L_B, (Å)		L_B^*, (Å)		
		PA6	HDPE total	HDPE-iso	HDPE-orient.	PA6 orient.
1	90/10/0	100	223	224	222	95
2	80/20/0	90	229	225(231)	222(225)	86
3	77.5/20/2.5	94	221	224	211	91
4	75/20/5	94	220	224	213	92
5	70/20/10	87	215	225(245)	210(214)	88
6	65/30/5	82	236	223	231	77

Note: The values in parentheses were obtained after recrystallization of the HDPE by in-beam heating to 160°C followed by cooling down to 30°C

As already mentioned, after recrystallization, the HDPE fraction in the non-compatibilized and compatibilized samples became oriented differently; in the first case, the scattering maxima appeared on the meridian, whereas in the second, they maintained their position on the equator. As shown in Table 14.8, in both the 80/20/0 and 70/20/10 samples, an increase in the long spacing of isotropic HDPE, in the presence and absence of the compatibilizer, was observed after matrix recrystallization (the data are presented in parentheses).

Similar SAXS measurements were performed with PA12-reinfoced UDP MFCs. Figure 14.24 shows the SAXS patterns of three representative HDPE/PA12/YP UDP MFC compositions (after corrections for the empty chamber

scattering and for the intensity of the primary beam): without compatibilizer, (1) 80/20/0; with compatibilizer, (2) 70/20/10 and (3) 75/20/5 at different temperatures. It can be seen that at 30ºC the three MFC contain both isotropic scatterers, producing the circular reflection with an estimated L_B value of approximately 220 Å, and oriented ones giving rise to the two point-like reflections oriented along the horizontal axis of fibril orientation and with very similar L_B values (Table 14.9). The latter cannot belong to the reinforcing oriented PA12 whose typical L_B is in the range of 100–110 Å [78,101]. Therefore, it can only be attributed to the scattering of HDPE (or, in compatibilized systems, of LLDPE) oriented material crystallized upon the PA12 fibrils.

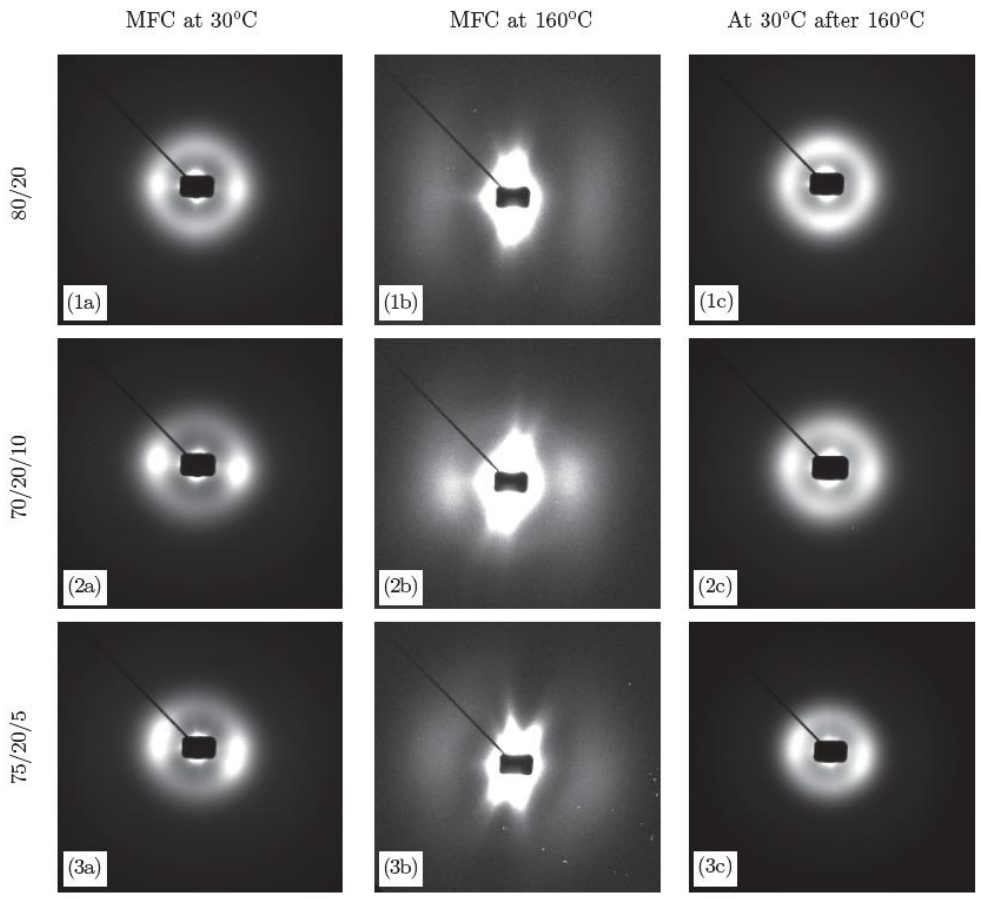

Figure 14. 24. 2D SAXS images of different HDPE/PA12/YP UDP MFC: column (a) – as prepared, at 30°C; column (b) – at 160°C, in-beam heating; column (c) – at 30°C after heating to 160°C (recrystallization) [64]

Table 14. 9. Bragg's Long spacing values of HDPE/PA12/YP UDP MFC at 30°C and after matrix recrystallization (at 30°C after melting at 160°C) [64]

HDPE/PA12/YP UDP MFC composition (wt%)	SAXS at 30°C				SAXS at 30° after 160°C			
	Isotropic scattering	Oriented scattering			Isotropic scattering	Oriented scattering		
	L_B HDPE (Å)	L_B^{Eq*} PE (Å)	L_B^{Mer*} PE (Å)	L_B^{Eq} PA12 (Å)	L_B HDPE (Å)	L_B^{Eq*} PE (Å)	L_B^{Mer*} PE (Å)	L_B^{Eq} PA12 (Å)
90/10/0	220	229	251	91	229	235	251	108
80/20/0	216	235	256	101	218	253	268	112
77.5/20/2.5	215	220	–	100	218	248	255	120
75/20/5	213	229	–	97	244	242	244	118
70/20/10	208	233	–	96	225	215	229	124
65/30/5	218	229	–	99	218	250	265	118

Note: L_B^{Eq*} – long spacing of the PE lamellae oriented along the equator; L_B^{Mer*} – long spacing of the PE lamellae oriented along the meridian. The fiber direction coincides with the equator. Oriented PE includes fractions of the matrix HDPE or LLDPE of YP

The oriented reflections of PA12 can be visualized only after the matrix melting at 160ºC (Figure 14.24, second column). While the L_B of the sample without compatibilizer (pattern 1b) is consistent with the neat PA12, that of the sample containing 5 and 10% compatibilizer shows scattering with larger L_B of 120 and 130 Å, respectively. Most probably, these oriented reflections in patterns 2b and 3b at 160ºC originate from LLDPE/MAH-co-PA12 block copolymer obtained through the reaction of the YP and PA12, being still crystalline and oriented at 160ºC. The SAXS patterns obtained at 30 and 160ºC give a strong evidence of the presence of oriented PE in the final MFCs, thus proving the shell-core morphology of the reinforcing fibers, comprising a core of oriented PA12 with a shell of oriented, transcrystalline PE (HDPE or LLDPE).

It is interesting to compare the SAXS patterns of the three starting MFCs at 30ºC (Figure 14.24, column 1) and those obtained after their recrystallization carried out in the beam (30ºC after 160ºC), (column 3). They are not identical. It can be seen that upon recrystallization meridional point-like reflections (*i.e.*, perpendicular to the axis of fiber alignment) also appear, better seen in the non-compatibilized sample meridian (45–135º) for L_B^{Mer*} (Table 14.9). Also, in the as-prepared MFCs a periodicity of PE along the equator with L_B^{Eq} is always present, fluctuating around 230 Å independently of the YP content, whereas meridional reflections with L_B^{Mer*}>250 Å only appear in the non-compatibilized MFCs. Changes toward increasing of both PE periodicities occur upon matrix recrystallization. Generally, the PE lamellae along the meridian have bigger long spacings as compared to those of the PE crystallized along the fiber direction. The PA12 long spacings L^{Eq} are between 90 and 100 Å in the MFC prior to

recrystallization, which is in good agreement with the values of the neat oriented PA12 [101]. After recrystallization a significant growth of L_B^{Eq} is registered; between 11 Å in the 80/20/0 MFC and 28 Å in the YP-reach 70/20/10 MFC. It seems that compatibilization results in changes in both PE and PA12 components. These changes become clearer which in the SAXS patterns after matrix recrystallization.

Additional information can be extracted from the SAXS patterns of the UDP MFCs based on a recently developed automated treatment procedure [102]. The 2D SAXS patterns of the UDP MFCs are background-corrected, intensity-calibrated and digitally reconstructed. Thereafter, the scattering from the oriented and isotropic scatterers is separated and used to calculate the Chord Distribution Function (CDF) [103], representing a transformation to the real space of the respective SAXS pattern. Figure 14.25 shows the CDFs of the oriented scattering of HDPE/PA6/YP MFCs with compositions of 80/20/0 (image a) and 70/20/10 (image b).

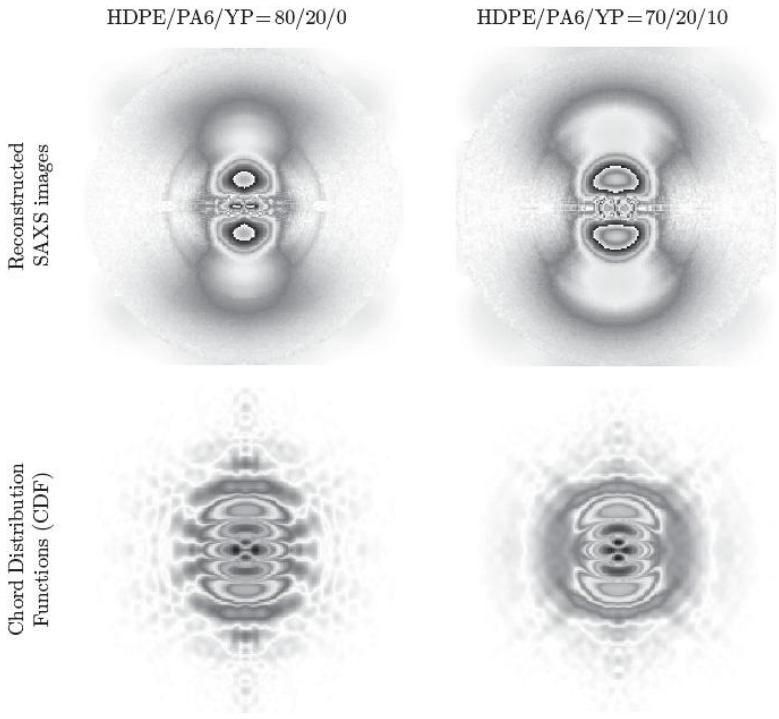

Figure 14. 25. Reconstructed SAXS patterns (oriented scattering) of two UDP MFC materials and their respective chord distribution functions. Fibril axis is vertical. The CDF function is presented in absolute values (both positive and negative faces in one image)

It is important to note that the CDF images reflect mostly the structure of the HDPE oriented TCL and to a lesser extent that of the PA6 fibrils. In addition to

the L_B values almost coinciding with those in Table 14.8, the CDF analysis of the two samples in Figure 14.25 showed that in the non-compatibilized sample (80/20/0) the HDPE TCL forms a microfibrillar system with first and second order long periods, with the HDPE domains being side-by-side and not shifted. Introducing compatibilizer (70/20/10 sample) maintains these structural features but results in the appearance of tilted oriented HDPE domains. The biggest advantage of this data treatment procedure is that it can be applied to the large datasets originating from simultaneous synchrotron SAXS-straining experiments significantly improving the speed of processing, and the SAXS data quality, as well as allowing the registration and interpretation of deformations at nanoscale not accessible at this point. All these advantages were recently demonstrated with HDPE/PA/YP oriented precursor cables [104] associating the nanostructural features with the simultaneously obtained mechanical behavior in stretching or load cycling modes.

14.4.2.2. *Wide-angle X-ray scattering*

Both SEM and SAXS studies of UDP MFC materials reinforced by PA6 or PA12 fibrils gave evidence that the reinforcing fibrils most probably have a layered, coaxial structure: a core of oriented PA and a shell of oriented, transcrystalline HDPE. The WAXS measurements supported and allowed a further development of this hypothesis.

The visual inspection of the WAXS patterns of HDPE/PA6/YP UDP MFCs (Figure 14.26) shows that the crystallographic characteristics of HDPE and PA6 are very similar, leading to a strong overlapping of the respective diffraction peaks. Nevertheless, one can notice that at 30ºC there is a co-existence of isotropic Debye rings and oriented crystalline reflections. At 160ºC the HDPE reflections change into a diffuse amorphous halo revealing the oriented PA6 reflections.

To separate the contribution of the isotropic and oriented crystalline fractions and to study their origin, the same subtraction procedure as with the SAXS patterns was applied. Figure 14.27 exemplifies this treatment for the 80/20/0 (a) and 70/20/10 (b) HDPE/PA6/YP UDP MFCs showing the starting real 2D WAXS patterns (left), the computer-generated isotropic part of the scattered intensity (center) and the resulting 2D WAXS images of the oriented part after subtraction (right). Subtracting the isotropic crystalline and amorphous fractions allows the outlining of the oriented crystalline reflections that are otherwise undetectable. Together with the expected oriented PA6 reflections in the right images in Figure 14.27, one observes also clear reflections of the oriented matrix. The two weak equatorial arcs belong to the (200) plane (the internal arc) and the (002/202) planes (the external arc) of PA6 and the other two, more intense equatorial reflections, belong to the (110) plane (internal reflection) and (200) planes (external reflection) of orthorhombic unit cell of HDPE. This is another

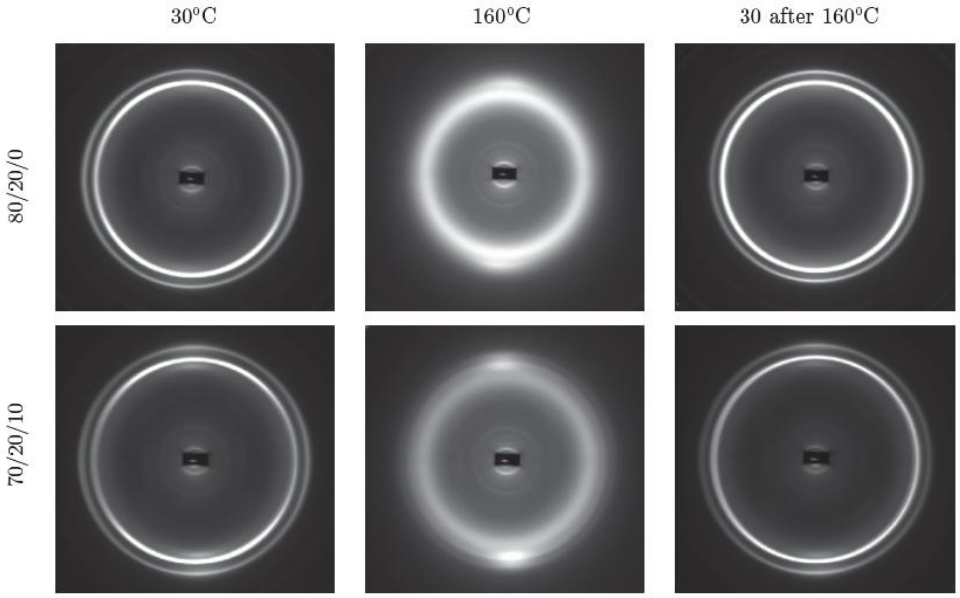

Figure 14.26. 2D WAXS patterns of HDPE/PA6/YP microfibrillar composites taken at various temperatures. Fibril direction is horizontal [63]

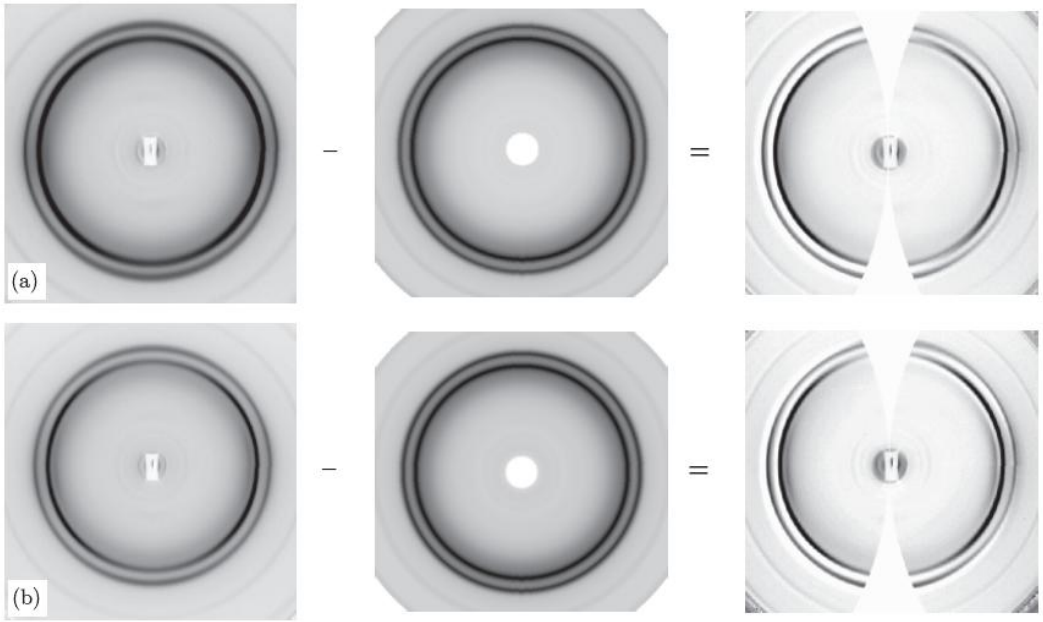

Figure14..27. Example of the analysis of the WAXS patterns at 30°C of HDPE/PA6/YP UDP MFCs: Left – total scattered intensity; Center: calculated isotropic intensity; Right: oriented scattered intensity. (a) 80/20/0 and (b) 70/20/10. The fiber axis is vertical [63]

indication for epitaxial crystallization of matrix material upon the reinforcing fiber, whereby the chain direction in the matrix crystals coincides with that in the reinforcing PA6 fibrils. Judging from Figure 14.27, this observation is valid for both selected samples – non-compatibilized (a) and compatibilized (b).

Figure 14.28 shows the 3D images of the real WAXS patterns before treatment (left) and of the oriented scattering after subtracting (right) of the 80/20/0 and 70/20/10 MFCs. The white arrows indicate the position of the α-PA6 (200) reflection. This representation shows better the anisotropy of the HDPE (110) and (200) reflections. For a quantitative evaluation of oriented and isotropic parts of the total scattered intensities, the respective 2D WAXS patterns were integrated in the 0–180° range to get the 1D WAXS profiles, which were afterwards fitted by Gaussian peaks.

The results from peak-fitting applied in the 80/20/0 MFC sample are presented in Figure 14.29a and b. The deconvolution of the integral profile of the oriented part clearly shows the (110), (200) and (210) contributions of the HDPE (Figure 14.29a, the shaded reflections) and also the four crystalline reflections of α- and γ-PA6. The peak-fitting of the isotropic part displayed crystalline reflections (110), (200) and (210) of the HDPE matrix only and the amorphous halos of PA6 and HDPE, respectively (Figure 14.29b).

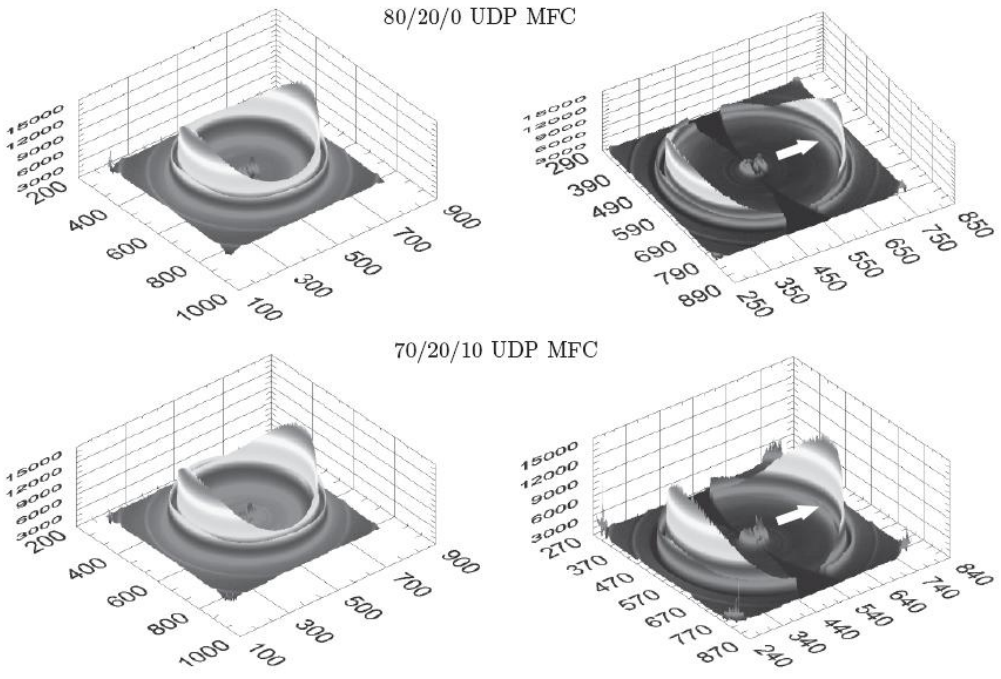

Figure 14.28. 3D WAXS patterns of UDP MFCs before (left) and after (right) subtraction of the azimuthally independent component of the total scattered intensity. The white arrows point at the (200) reflection of α-PA6 [63]

Based on the angular position of the reflections, the *d*-spacings (d_{hkl}) of the corresponding planes were calculated. A quantitative evaluation of the peak-fitting results for two representative MFCs – without (80/20/0) and with compatibilization (70/20/10), as well as data for *d*-spacings are given in Table 14.10. It can be seen that a significant part of the HDPE matrix is able to crystallize oriented along the PA6 fiber thus forming a transcrystalline layer in such a way that the chain directions of the two polymers coincide.

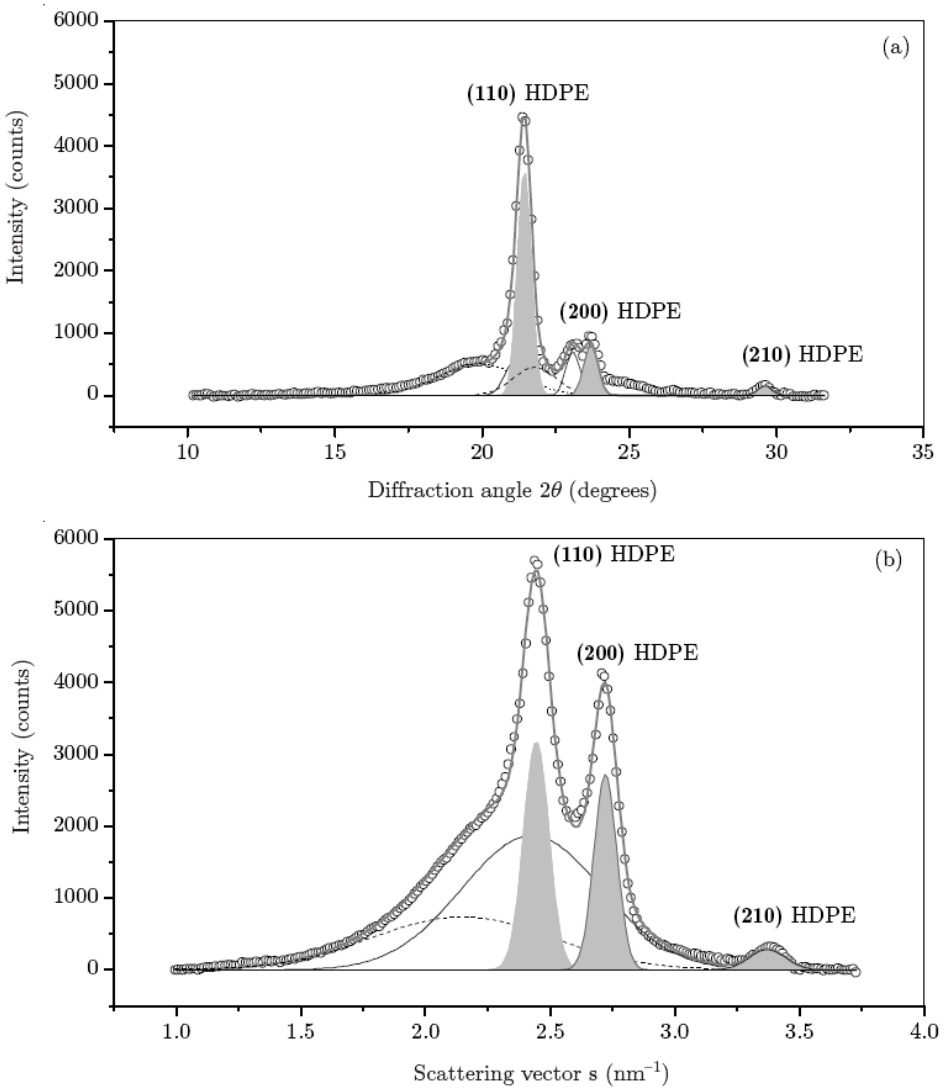

Figure 14. 29. 1D WAXS profiles of the 80/20/0 HDPE/PA6/YP UDP MFC exemplifying the peak-fitting of the oriented scattering (a) and of the isotropic WAXS scattering (b) [63]

The rest of the matrix, situated in the bulk, crystallizes isotropically. The relation between the content of the PA6 fibrils and the oriented part of the HDPE matrix (the crystalline fraction) is almost 1.03:1.00 in the 70/20/10 MFC and 1.26:1.00 in the 80/20/0 system. This means that in the presence of compatibilizer a larger part of the HDPE is included in the transcrystalline layer without changing considerably its crystallographic characteristics. Based on the *d*-spacing values, it can be concluded that the HDPE unit cell is slightly larger in the bulk, as compared to that in the oriented transcrystalline layer.

Table 14..10. Results from the deconvolution of the oriented and isotropic part of 2D WAXS patterns of selected HDPE/PA6/YP UDP MFC [63]

WAXS Reflections	HDPE/PA6/YP					
	80/20/0			70/20/10		
	2θ, (deg.)	Content, (%)	d_{hkl}, (Å)	2θ, (deg.)	Content, (%)	d_{hkl}, (Å)
	Oriented part of WAXS intensity					
(200) α PA6	19.90	28.5	4.34	19.92	28.7	4.34
(001) γ PA6	21.05	6.6	4.11	21.35	7.6	4.07
(110) – HDPE	21.44	34.9	4.03	21.33	38.2	4.05
(200) γ PA6	21.79	13.7	3.97	21.66	7.6	3.99
(002)/(202) α PA6	23.09	6.9	3.75	22.99	6.9	3.76
(200) – HDPE	23.69	7.9	3.65	23.74	9.1	3.65
(210) – HDPE	29.61	1.5	2.94	29.50	1.9	2.95
PA6 fraction, %		55.7			50.8	
HDPE fraction, %		44.3			49.2	
	Isotropic part of WAXS intensity					
(110) – HDPE	21.13	14.6	4.09	20.97	9.8	4.12
(200) – HDPE	23.56	11.4	3.67	23.48	12.6	3.69
(210) – HDPE	29.29	1.9	2.96	29.24	1.3	2.97

Notes: In the isotropic part of the WAXS intensity the crystalline reflections are only included. The difference to 100% will give the content of the amorphous HDPE and amorphous PA6. d_{hkl} is the *d*-spacing of the respective crystalline plane. The oriented reflections are assumed 100% crystalline.

The same WAXS measurements were performed with the HDPE/PA12/YP unidirectional MFCs just like with the PA6-reinforced systems. Figure 14.30 displays 2D WAXS patterns of HDPE/PA12/YP MFC with unidirectional alignment of the reinforcing fibrils, with and without compatibilizer at 30ºC, 160ºC and 30ºC after matrix recrystallization at 160ºC. Judging from the two point-like reflections close to the center of the patterns, ascribed to the γ-PA12 (0k0) planes that appear at the three temperatures, it can be concluded that under these

conditions there exist significant amounts of γ-PA12 polymorph. The two Debye rings in the patterns at 30ºC should be related to the presence of isotropic HDPE, whose (110) plane (the internal ring) and (200) plane (the external one), are super imposed with the equatorial PA12 oriented reflections characterizing its (001) and (200) planes.

To study the crystalline structure of the PA12 core of the fibrils, the 2D WAXS patterns at 160ºC were sectioned and the respective 1D profiles deconvoluted by peak fitting. Figure 14.31 exemplifies the fit of the 70/20/10 UDPE MFC at 160ºC. There is overlapping of many reflections in the 2θ range studied, but with the help of the results obtained from the detailed investigation on neat PA12 [78,101] their identification was possible in the MFC. The deconvoluted reflections of the two PA12 polymorphs in the order of increasing 2θ are as follows: γ(020); α(100); γ(040); α(200); γ(001); γ(200); α(002). As seen from Figure 14.31, there exist considerable amounts of α-PA12 polymorph (the shaded peaks) in the 70/20/10 MFC. Table 14.11 summarizes the polymorph composition of all HDPE/PA12/YP UDP MFC at 160ºC obtained analogously.

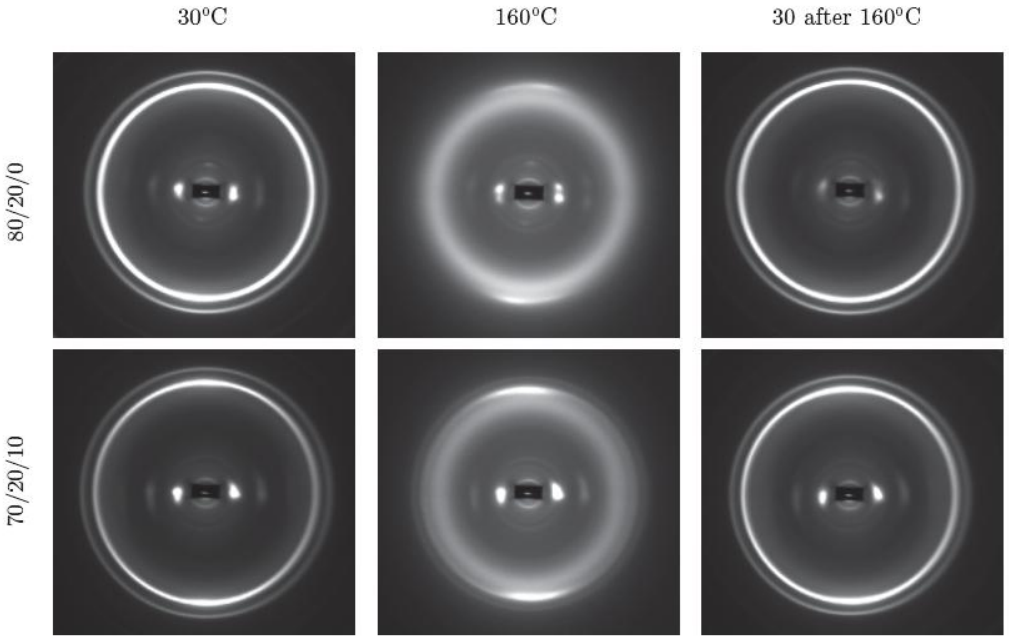

Figure 14.30. 2D WAXS patterns of HDPE/PA12/YP UDP MFC taken at various temperatures. Fiber axis is horizontal [64]

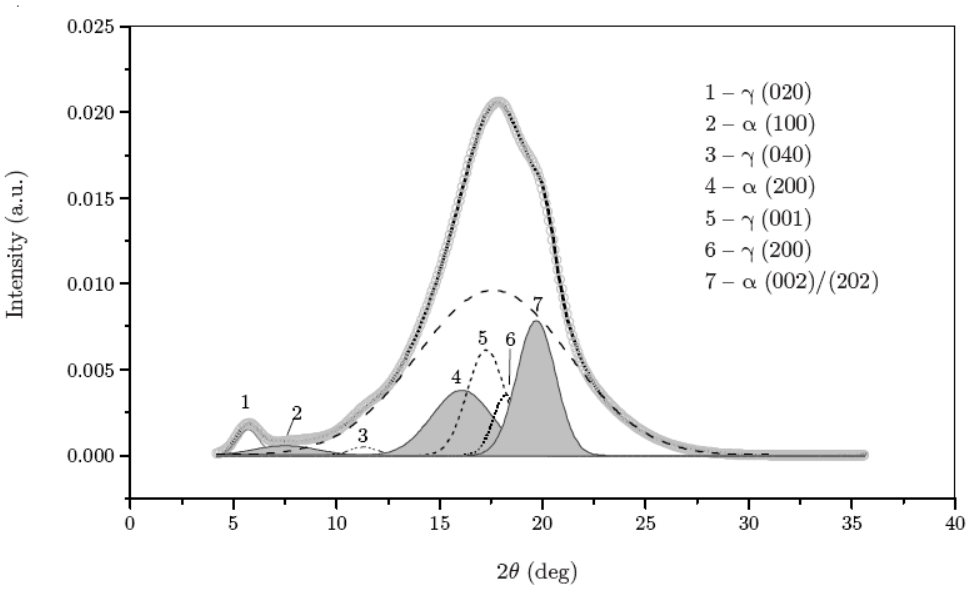

Figure 14.31. Peak-fitting of 1D WAXS curve of the 70/20/10 UDP MFC at 160°C. The shaded peaks belong to α-PA12. The broad peak centered at $2\theta = 18^{\circ}$ originates from the diffuse scattering of the amorphous material [64]

Table 14.11. PA12 polymorph content in HDPE/PA12/YP MFC at 160°C [64]

Composition HDPE/PA12/YP (wt%)	Vol. fract. of PA12, (%)	α form, (%)	γ form, (%)	α/γ	CI, (%)
90/10/0	0.094	11.3	23.8	2.10	35.1
80/20/0	0.189	16.9	25.0	1.48	41.9
70/20/10	0.188	23.7	15.4	0.65	39.1
75/20/5	0.189	19.6	23.7	1.20	43.3
77.5/20/2.5	0.189	20.0	21.2	1.06	41.2
65/30/5	0.285	20.5	20.7	1.01	41.2

Notes: CI = crystallinity index. CI = αCI + γCI; αCI = α(100) + α(200) + α(002); γCI = γ(020) + γ(040) + γ(001) + γ(100)

Table 14.11 shows that the crystallinity index of the PA12 fibrils at 160ºC varies between 35–43% comprising different proportions of α and γ-PA12. The γ/α ratio is the biggest (γ/α = 2.1) in the 90/10/0 composition. Within the samples

containing 20% PA12, the γ polymorph is predominant in the 80/20/0 system (γ/α = 1.48), while the 70/20/10 composite containing the biggest YP concentration, *i.e.*, largest amounts of LLDPE chemically attached to PA12, is richer in α-PA12 form (γ/α = 0.65).

To study the WAXS patterns of the as-prepared PA12-reinforced MFCs at 30ºC trying to evaluate the TCL, the total scattered intensity was separated into two contributions using the same software and procedures as described above. The final results of this subtraction procedure are displayed in Figure 14.32, where the oriented WAXS scattering of two typical patterns of MFC without (a) and with compatibilization (b) are presented. One can observe the anisotropy of the (110) and (200) PE reflections, as well as some of the oriented equatorial and meridional reflections of the PA12: 1 – α(100); 2 – γ(020); 3 – γ(040); 4 – α(200). It should be noted that the chain direction of PA12 and that of the oriented PE fraction coincide in both compatibilized and non-compatibilized HDPE/PA12/YP MFC. This is true not only in the as-prepared MFC at 30ºC (Figure 14.32), but also for MFC samples after recrystallization at 160ºC.

Figure 14.33 shows the peak-fitted 1D WAXS profiles of a compatibilized MFC sample (HDPE/PA12/YP = 70/20/10). As seen from the deconvolution of the oriented scattering (Figure 14.33a), the main reflections of the PE (shaded peaks) overlap with those of the α-PA12 (peaks 5 and 9) and γ-PA12 polymorphs (peaks 6 and 8). Altogether, the following reflexes were identified (given in increasing 2q order): γ-PA12(020); α-PA12(100); γ- PA12(040); γ-PA12(060); α-PA12(200); γ-PA12(001); PE(110); γ-PA12(200); α-PA12(002); PE(200); PE(210). The peak-fitting of the isotropic part (Figure 14.33b) displayed crystalline reflections only of the HDPE matrix, indexed as (110), (200) and (210), along with the amorphous halos of PA12 and HDPE.

The WAXS patterns of all MFC were treated analogously. The data in Table 14.12 show that in all compositions investigated there exists a part of PE that crystallizes orientated along the PA12 fibrils. The percentage of this part varies between 26% and 35% of the total oriented scattering and depends on the PA12 concentration – it is the highest in the sample with 10% PA12, and the lowest in the 65/30/5 composition. Assuming that PA12 is 100% fibrillar, the fraction of the oriented polyethylene [PE]* in the respective MFC can be calculated. It can be seen that the [PE]* increases as the PA12 content grows from 10 to 30%. Another observation is that the YP concentration also has some influence – the bigger the YP content, the larger is the [PE]* amount that crystallizes oriented along the PA12 fibrils.

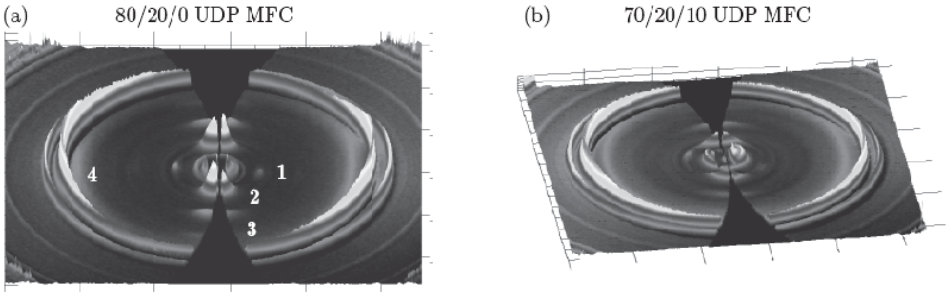

Figure 14.32. Fraser corrected 3D WAXS patterns at 30°C after subtraction of the isotropic component of: (a) 80/20/0 MFC UDP, and (b) 70/20/10 MFC UDP. The numbers indicate the following PA12 crystalline planes: 1 – α(100); 2 – γ(020); 3 – γ(040); 4 – α(200). The fiber axis is vertical [64]

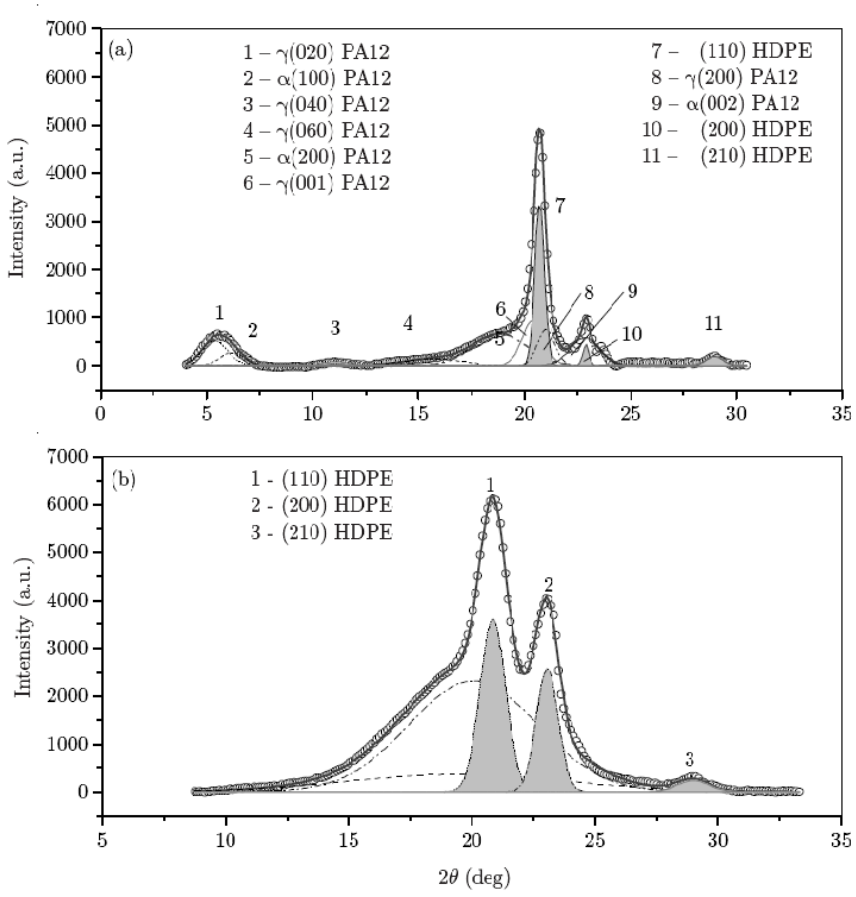

Figure 14. 33. 1D WAXS profiles of the 70/20/10 HDPE/PA12/YP UDP MFC depicting the peak-fitting of the oriented WAXS scattering (a) and of the isotropic WAXS scattering (b) [64]

Table 14.12. Results from the deconvolution of the oriented part of 2D WAXS patterns of HDPE/PA12/YP UDP MFC [64]

Composition HDPE/PA12/YP (wt%)	α-PA12 (%)	γ-PA12 (%)	PA12 total (%)	HDPE (oriented) (%)	*f*	[HDPE]* (oriented) (wt%)
90/10/0	21.7	43.6	65.3	34.7	1.883	5.31
80/20/0	42.2	31.6	73.8	26.2	2.817	7.10
70/20/10	28.9	37.1	66.0	34.0	1.942	10.30
75/20/5	13.2	54.2	67.4	32.6	2.066	9.68
77.5/20/2.5	19.9	49.0	68.9	31.1	2.217	9.02
65/30/5	23.8	47.3	71.1	28.9	2.463	12.19

Notes: The coefficient *f* is the relationship between the PA12 and HDPE fractions of the oriented scattering; The [HDPE]* (oriented) represents the oriented part of the PE material (matrix HDPE and/or LLDPE from YP) if the PA12 is assumed to be 100% oriented

14.4.2.3. *Evaluation of the TCL thickness*

The combination of data from SEM and WAXS analyses allowed the approximate estimation of the TCL thickness. According to the model in Figure 14.19, the reinforcing fibril in the final MFC is cylindrical, comprising a core of oriented PA and a coaxial shell of oriented HDPE (Figure 14.34A). It can be seen that (Eq. 14.7 and 14.8):

$$V_{PA} = \pi R_1^2 . L \text{ and}$$

$$V_{TCL} = \pi L (R_2^2 - R_1^2)$$

where R_2 is the outer (*i.e.*, visible by SEM) radius of the fibril, and R_1 is the radius of the PA core. V_{PA} and V_{TCL} are the volumes of the PA and transcrystalline oriented HDPE, respectively. Each of the two volumes will be proportional to the respective part of the oriented WAXS intensity, *i.e.* (14.9.)

$$I_s^{PA} \sim V_{PA} . \rho_{el}^{PA} \text{ and } I_s^{HDPE} \sim V_{HDPE} . \rho_{el}^{HDPE}$$

Here, ρ_{el} represents the volume average electron density of PA (PA6 or PA12) and HDPE calculated in the following way (14.10) [105]:

$$\rho_{el} = N_A . \frac{Z_M}{M_M} . \rho_m \text{ , [electron units/nm}^3\text{]}$$

N_A being the Avogadro's number, Z_M – the number of electrons per repeat unit, M_M –molecular weight of the repeat unit, and ρ_m – the average mass density. The average electron densities of HDPE, PA6 and PA12 were found to be 347, 376 and 339 eu/nm^3, respectively.

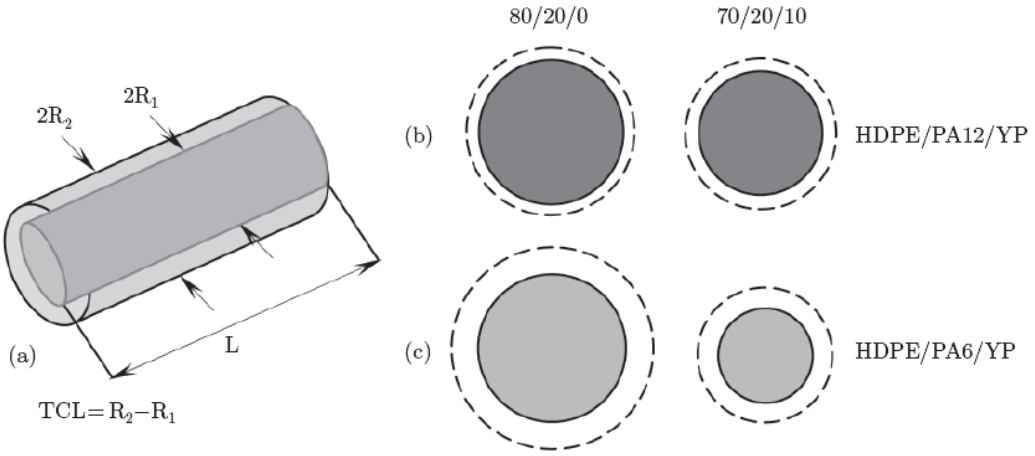

Figure 14.34. Idealized model of the PA reinforcing fibril: (a) representation of core, shell and TCL thicknesses, (b) and (c) to-scale representations of the cross-sections of the PA12 and PA6 reinforcing fibril in two HDPE/PA/YP MFCs: 80/20/0 and 70/20/10. The solid circles represent the polyamide fibers, and the dashed circles – the trans-crystalline HDPE layer. For more details see the text [64]

After dividing Eq. (7) by Eq. (8) and rearrangement, the following expression is obtained (14.11):

$$2R_1 = 2R_2 \cdot \sqrt{\frac{f}{k+f}}$$

wherein f is the relationship between the PA and HDPE fractions of the oriented scattering (Tables 14.10 and 14.12) and $k=\rho^{el}_{PA}/\rho^{el}_{HDPE}$. Using Eq. (11), the TCL thicknesses in all MFC under investigation were calculated and also the real AR of the PA12 reinforcing fibrils, *i.e.*, after elimination of the thickness of the HDPE shell (Table 14.13). It should be noted that the real AR values almost coincide with those obtained after selective extraction of the HDPE component (Table 14.2, last column), which is a corroboration of the credibility of the methods for TCL estimation applied.

From Table 14.13 it can be also seen that the TCL in the HDPE/PA12/YP composites varies in the 43–96 nm range, being the finest in the samples without

compatibilizer, the same showing also the largest fibril length, *L*. Generally, compatibilization in PA12-reinforced UDP composites results in an increase of TCL and in a more pronounced decrease of *L*. Figure 14.34B visualizes the cross-sections of these fibrils in two selected HDPE/PA12/YP samples without and with compatibilizer. For the 80/20/0 sample $2R_2/2R_1$/TCL = 625/539/43 nm. In the compatibilized sample (70/20/10), the core and the total diameters decrease, while the TCL grows with 9 nm and $2R_2/2R_1$/TCL =560/456/52 nm. The cross-sections of the respective HDPE/PA6/YP determined analogously are characterized by larger TCL thicknesses, especially in the non-compatibilized 80/20/0 sample with TCL=100 nm. The addition of 10% of compatibilizer in PA6-reinforced MFC results in a decrease of TCL thickness to 75 nm and in much stronger drop of the AR (Table 14.13).

Table 14. 13. Relationship between some structural parameters of the reinforcing fibrils in HDPE/PA/YP MFC as revealed by SEM and WAXS studies and the mechanical properties of the respective material

Sample composition, (wt%)	$2R_2$, (nm)	$2R_1$, (nm)	TCL, (nm)	L, (μm)	AR	Real AR	Tensile strength ó, (MPa)	Young's modulus, (MPa)	Flexural stiffness, IP, (%)
HDPE/PA6/YP UDP MFC									
80/20/0	750	550	100	50.8	68	92	57±4	1095±52	53.4
70/20/10	500	350	75	4.6	9	13	37±2	920±37	48.7
HDPE/PA12/YP UDP MFC									
80/20/0	625	539	43	52.0	83	97	64±3	1054±37	104.3
70/20/10	560	456	52	33.2	59	73	55±6	972±47	97.1
65/30/5	1250	1058	96	53.3	43	50	33±4	1030±43	98.4

Notes: $2R_2$ – fibril diameter visible by SEM; $2R_1$ – diameter of the PA6 or PA12 core calculated by Eq. (11); TCL= thickness of the oriented HDPE shell; L= estimated length of the PA fibril; visible AR= L/R2; Real AR= L/R_1.

It will be of some interest to relate the thickness and morphology of the TCL to the mechanical properties of the MFC materials with either PA6 or PA12 fibril reinforcement (Table 14.13). It can be concluded that in the HDPE/PA6/YP UDP MFCs, compatibilization resulted in thinner and shorter fibrils in which both the PA6 core and the HDPE TCL were finer. The significantly lower AR in the YP containing HDPE/PA6 composites drastically decreased the tensile and impact strength in respect to the non-compatibilized composite, but the flexural stiffness was almost unaffected. As regards the PA12-reinforced MFCs, again the best mechanical properties were related with the highest AR values. Interestingly, the tensile and flexural properties of the 80/20/0 PA12-reinforced composite were notably better than of the PA6-analogue. Table 14.13 shows that this effect can be related with the significantly thinner TCL in the PA12-reinforced MFC. This

thinner HDPE coating affects less negatively the way the load is transferred from the matrix to the PA12 reinforcing fibrils, especially if the AR remains constant.

In conclusion of this subsection, let us mention that studying the TCL in MRB and NOM composites by the reported SAXS/WAXS procedure is impossible because of the lack of a preferred orientation.

14.5. Conclusions and outlook

Nowadays conventional polymer composites are important commercial materials with a wide range of applications in many industries (*e.g.*, aerospace, automotive, *etc*.) where highly resistant and lightweight materials are of prime importance. In recent years, however, optimizing the properties of the traditional polymer composites containing micrometerscale reinforcing entities has reached its limits. The micro- and nanosized fibrillar composites open a large window of opportunities to further improve the mechanical properties. The results shown in this chapter confirm the concept that changing the size, shape, alignment, volume fraction, interface, and degree of dispersion of the reinforcements is a way to understand, tailor, and optimize the composites' mechanical properties.

Based on the critical evaluation of the results on various MFCs, it can be inferred that additional reinforcing effect in the MFC systems can be expected if layered, fibrillar or particulate nanosized inorganic fillers are introduced into either the reinforcing fibrils or in the matrix of MFC and dispersed to nanometer-scale, maintaining the high orientation of the reinforcements. This can be one of the future lines of investigation in this area employing nanotubes, montmorillonite, *in situ* produced nanoparticles of silica, TiO_2, *etc*. Different types of compatibilizers can be used in such hybrid (*i.e*., organic-inorganic) materials. The hyperbranched or dendritic polymers possess a high content of functional groups, which could be modified arbitrarily in order to obtain additional effects on the physical properties or to change the reactivity for further chemical reactions. Very recently, a new trend toward *in situ* polymer-polymer composites is observed, namely the molecular dispersion of one polymer in another. The synthetic principle is simple – the reinforcing polymer is dissolved in the monomer of the matrix and then the latter is polymerized by means of adequate initiators. In general, *in situ* polymerization seems to have a bright future as far as new polymer nanocomposites are concerned.

The studies on MFCs demonstrated also that synchrotron WAXS and SAXS methods can be very useful in studying the relation between the structure and the mechanical properties of polymer composites. The progress in X-ray experiments during the last years has been tremendous and included development of new two-dimensional X-ray detectors, the use of high power X-ray microbeams, and the application of novel processing methodologies allowing for a direct transformation of the WAXS and SAXS 2D patterns into real-space images of the nanostructure.

All this will enable real time X-ray experiments using mechanical testers for slow or fast load-cycling test incorporated into the synchrotron beamline. In this way, fatigue and failure can be studied in MFC within reasonable intervals of time and the data obtained will be related to microstructure variation inside the material. These advanced methods may become of some importance in both applied and academic studies with the advent of various types of nanostructure manipulations, all of them requiring a strict control over the morphologies on the nanometer scale and well-known structure-properties relations.

Acknowledgements The authors gratefully acknowledge the financial support of the European Commission, Contract Grant Number HPRI-CT-2001-00140, and of HASYLAB at DESY (Grant Number II-07-011EC). N.D. is grateful to Fundação para a Ciência e Tecnologia (FCT) for supporting her research by post doctoral grant SFRH/BPD/45252/2008. Z.D. is grateful for the tenure of the FCT sabbatical grant SFRH/BSAB/812/2008 and for the hospitality of the Institute of Technical and Macromolecular Chemistry, Hamburg, where a part of this chapter was written.

References

1. Hull D and Clyne T W (1996) *Introduction to Composite Materials*, Cambridge University Press, Cambridge, UK, 2nd edition, p. 13.
2. Utracki L A (1989) *Polymer Alloys and Blends: Thermodynamics and Rheology*, Hanser Publishers, Munich, Vienna, New York, p. 43.
3. Schadler L S (2003) Polymer-based and Polymer-filled Nanocomposites, in *Nano-composite Science and Technology* (Eds. Ajayan P M, Schadler L S and Braun P V), pp. 77–144.
4. Usuki A, Kojima Y, Kawasumi M, Okada A, Fukushima Y, Kurauchi T and Kamigato O (1993) Synthesis of nylon 6-clay hybrid, *J Mater Res* **8**:1179–1184.
5. Yano K, Usuki A, Okada A, Kurauchi T and Kamigaito O (1993) Synthesis and properties of polyimide-clay hybrid, *J Polym Sci A: Polym Chem* **31**:2493–2498.
6. Giannelis E P (1998) Polymer-layered silicate nanocomposites: Synthesis, properties and applications, *Appl Organomet Chem* **12**:675–680.
7. Ray S S and Okamoto M (2003) Polymer/layered silicate nanocomposites: a review from preparation to processing, *Prog Polym Sci* **28**:1539–1641.
8. Mark J E (2006) Some novel polymeric nanocomposites, *Acc Chem Res* **39**:881–887.
9. Evstatiev M, Fakirov S, Bechtold G and Friedrich K (2000) Structure-property relationships of injection- and compression-molded microfibrillar-reinforced PET/PA6 composites, *Adv Polym Technol* **19**:249–259.
10. Chakraborty S, Sahoo N G, Jana G K and Das C K (2004) Self-reinforcing elastomer composites based on ethylene–propylene–diene monomer rubber and liquid-crystalline polymer, *J Appl Polym Sci* **93**:711–718.
11. Tjong S C (2003) Structure, morphology, mechanical and thermal characteristics of the *in situ* composites based on liquid crystalline polymers and thermoplastics, *Mater Sci Eng* **41**:1–60.
12. Song C H and Isayev A I (2001) LCP droplet deformation in fiber spinning self-reinforced composites, *Polymer* **42**:2611–2619.
13. Handlos A A and Baird D G (1996) Injection molding of microcomposites based on polypropylene and thermotropic liquid crystalline polymers, *Int Polym Proc* **11**:82–93.
14. Evstatiev M and Fakirov S (1992) Microfibrillar reinforcement of polymer blends, *Polymer* **33**:877–880.
15. Evstatiev M, Fakirov S and Schultz J M (1993) Microfibrillar reinforced composite from drawn poly(ethylene terephthalate)/nylon-6 blend, *Polymer* **34**:4669–4679.
16. Fakirov S, Evstatiev M and Friedrich K (2002) Nanostructured Polymer Composites from Polymer Blends: Morphology and Mechanical Properties, in *Handbook of Thermoplastic Polyesters* (Ed. Fakirov S), Wiley-VCH, Weinheim, Germany, pp. 1093–1132.
17. Schaefer D W and Justice R S (2007) How nano are nanocomposites?, *Macromolecules* **40**:8501–8517.
18. Denchev Z and Dencheva N (2008) Transforming polymer blends into composites: a pathway towards nanostructured materials, *Polym Int* **57**:11–22.
19. Fakirov S, Evstatiev M and Friedrich K (2000) From polymer blends to microfibrillar reinforced composites, in *Polymer Blends*, vol. 11, (Eds. Paul D R and Bucknall C B), Wiley, New York, pp. 455–476.
20. Fakirov S, Evstatiev M and Friedrich K (1998) Microfibrillar reinforced composites from polymer blends, in *Polymerwerkstoffe 1998: Verarbeiterung, Anwendung, Recycling* (Eds. Radusch H J and Vogel J) Martin-Luther-Universität, Halle-Wittenberg, Halle/Saale, pp. 123–156.

21. Evstatiev M, Fakirov S and Friedrich K (2000) Microfibrillar reinforced composites: another approach to polymer blends processing, in *Structure Development During Polymer Processing* (Eds. Cunha A M and Fakirov S) Kluwer Academic, Dordrecht, Boston, London, pp. 311–325.
22. Evstatiev M, Fakirov S and Friedrich K (2005) Manufacturing and characterization of microfibrillar reinforced composites from polymer blends, in *Polymer Composites: From Nano- to Macroscale* (Eds. Friedrich K, Fakirov S and Zhang Z) Springer, New York, 149–167.
23. Shields R J, Bhattacharyya D and Fakirov S (2008) Fibrillar polymer-polymer composites: Morphology, properties and applications, *J Mater Sci* **43**:6758–6770.
24. Denchev Z, Evstatiev M, Fakirov S, Friedrich K and Pollio M (1998) Microfibrillar reinforced composites: the role of the chemical interactions at the fibril-matrix interface, *Adv Comp Mater* **7**:313–324.
25. Denchev Z, Kricheldorf H R and Fakirov S (2001) Sequential reordering in condensation polymers, 6. Average block lengths from NMR analysis in PET/PA6 copolymers as revealed by NMR, *Macromol Chem Phys* **202**:574–586.
26. Denchev Z, DuChesne A, Stamm M and Fakirov S (1998) Sequence length determination in poly(ethylene terephthalate)-bisphenol-A polycarbonate random copolymers by application of selective degradation, *J Appl Polym Sci* **68**:429–440.
27. Denchev Z, Bojkova A, DuChesne A, Höcker H, Keul H and Fakirov S (1998) Sequential reordering in condensation polymers, 5) Preparation via transreactions and characterization of copolymers based on poly(caprolactone)–poly(2,2-dimethyl trimethylene carbonate) blends, *Macromol Chem Phys* **199**:2153–2164.
28. Kricheldorf H R and Denchev Z (1999) Chemistry of transreactions in condensation polymers: kinetics, mechanisms and peculiarities, in *Transreactions in Condensation Polymers* (Ed. Fakirov S) Wiley-VCH, Weinheim, pp. 1–78.
29. Denchev Z (2002) Chemical interactions in blends of condensation polymers involving polyesters, in *Handbook of Thermoplastic Polyesters: PET, PBT, PEN – Homopolymers, Copolymers, Blends and Composites* (Ed. Fakirov S) Wiley-VCH, Weinheim, pp. 757–808.
30. Fakirov S, Kamo H, Evstatiev M and Friedrich K (2005) Microfibrillar reinforced composites from PET/LDPE blends: Morphology and mechanical properties, *J Macromol Sci: Part B Phys* **B43**: 775–89.
31. Friedrich K, Ueda E, Kamo H, Evstatiev M, Krasteva B and Fakirov S (2002) Direct electron microscopic observation of transcrystalline layers in microfibrillar reinforced polymer-polymer composites, *J Mater Sci* **37**:4299–4305.
32. Li Z M, Yang M B, Lu A, Feng J M and Huang R (2002) Tensile properties of PET/PE *in situ* microfibrillar composites via slit die extrusion and hot stretching, *Mater Letters* **56**:756–762.
33. Li Z M, Yang M B, Huang R, Yang W and Feng J M (2002) PET/PE composite based on *in situ* microfibers formation, *Polym Plast Technol Eng* **41**:19–32.
34. Lin R J T, Bhattacharyya D and Fakirov S (2007) Morphology of rotationally molded microfibril reinforced composites and its effect on product performance, *Key Eng Mat* **334**:349–352.
35. Xu H S, Li Z M, Wang S J and Yang M B (2007) Rheological behavior of PET/HDPE *in situ* microfibrillar blends: Influence of microfibrils' flexibility, *J Polym Sci Part B: Polym Phys* **45**:1205–1216.
36. Li Z M, Xie B H, Huang R, Fang X P and Yang M B (2004) Influences of hot stretch ratio on essential work of fracture of *in situ* microfibrillar PET/PE blends, *Polym Eng Sci* **44**:2165–2173.
37. Li Z M, Yang W, Xie B-H, Huang R and Yang M-B (2004) Morphology and tensile strength prediction of *in situ* microfibrillar PET/PE blend fabricated via slit die extrusion-hot stretching-quenching, *Macromol Mat Eng* **289**: 349–354.

38. Li Z M, Li L B, Shen K Z, Yang M B and Huang R (2004) *In situ* microfibrillar PET/iPP blend via slit die extrusion, hot stretching, and quenching: Influence of hot stretch ratio on morphology, crystallization, and crystal structure of iPP at a fixed PET concentration, *J Polym Sci Part B: Polym Phys* **42**:4095–4106.
39. Zhong G J, Li Z M, Li L B and Mendes E (2007) Crystalline morphology of isotactic polypropylene (iPP) in injection molded poly(ethylene terephthalate) (PET)/iPP microfibrillar blends, *Polymer* **48**:1729–1740.
40. Jayanarayanan K, Thomas S and Joseph K (2008) Static and dynamic mechanical properties of *in situ* microfibrillar composites based on polypropylene/poly(ethylene terephthalate) blends, *Composites Part A* **39**:164–175.
41. Friedrich K, Evstatiev M, Fakirov S, Evstatiev O, Ishii M and Harrass M (2005) Microfibrillar Reinforced Composites from PET/PP Blends: Processing, Morphology and Mechanical Properties, *Compos Sci Technol* **65**:107–116.
42. Li Z M, Yang W, Li L-B, Xie B-H, Huang R and Yang M-B (2004) Morphology and non-isothermal crystallization of *in situ* microfibrillar PET/PP blend fabricated through slit-extrusion, hot-stretch quenching, *J Polym Sci Part B: Polym Phys* **42**:374–385.
43. Li Z M, Li L-B, Shen K-Z, Yang W, Huang R and Yang M-B (2004) Transcrystalline morphology of an *in situ* microfibrillar PET/PP blend fabricated through a slit extrusion hot stretching-quenching process, *Macromol Rapid Commun* **25**: 553–558.
44. Fuchs C, Bhattacharyya D and Fakirov S (2006) Microfibril reinforced polymer-polymer composites: application of Tsai-Hill equation to PP/PET composites, *Compos Sci Technol* **66**:3161–3171.
45. Karingamanna J, Sabu T and Kuruvilla J (2010) *In situ* microfibrillar blends and composites of PP and PET: Morphology and thermal properties, *J Polym Res DOI 10.1007/s10965-009-9384-6.*
46. Evstatiev M, Fakirov S, Krasteva B, Friedrich K, Covas J A and Cunha A M (2002) Recycling of PET as polymer-polymer composites, *Polym Eng Sci* **42**:826–835.
47. Taepaiboon P, Junkasem J, Dangtungee R, Amornsakchai T and Supaphol P (2006) *In situ* microfibrillar-reinforced composites of isotactic polypropylene/recycled poly(ethylene terephthalate) system and effect of compatibilizer, *J Appl Polym Sci* **102**:1173–1181.
48. Lei Y, Wu Q, Xu Y and Yao F (2009) Morphology and properties of microfibrillar composites based on recycled PET and HDPE, *Composites Part A* **40**:904–912.
49. Chatreenuwat B, Nithitanakul M and Grady B P (2007) The effect of zinc oxide addition on the compatibilization efficiency of maleic anhydride grafted HDPE compatibilizer for HDPE/PA6 blends, *J Appl Polym Sci* **103**:3871–3881.
50. Lin C, Sun H, Wang S, Huang J, Li J and Guo S (2010) In-process ultrasonic measurements of orientation and disorientation relaxation of HDPE/PA6 composites with compatibilizer, *J Appl Polym Sci* **116**:320–327.
51. Kamal M R, Jinnah I A and Utracki L A (1984) Permeability of oxygen and water vapor through polyethylene/polyamide films, *Polym Eng Sci* **24**: 1337–1347.
52. Beltrame P L, Castelli A, Pasquantonio M D, Canetti M and Seves A (1996) Influence of interfacial agents on the physicochemical characteristics of binary PE/PA and ternary PE/PP/PA6 blends, *J Appl Polym Sci* **60**:579–590.
53. Yeh J T, Huang S S and Chen H Y (2005) Barrier resistance of PE, PE/modified PA and blends of modified PA and ethylene vinyl alcohol bottles against permeation of polar and nonpolar mixed solvents, *J Appl Polym Sci* **97**:1333–1344.
54. Willis J M and Favis B D (1988) Processing-morphology relationships of compatibilized polyolefin/polyamide blends. Part I: The effect of an ionomer compatibilizer on blend morphology, *Polym Eng Sci* **28**:1416–1426.

55. Chandramouli K and Jabarin S A (1995) Morphology and property relationships in ternary blends of PE/PA6/compatibilizing agents, *Adv Polym Technol* **14**:35–46.
56. Utracki L A, Dumoulin M M and Toma P (1986) Melt rheology of HDPE/PA6 blends, *Polym Eng Sci* **26**:34–44.
57. Burger C, Hsiao B S and Chu B (2006) Nanofibrous materials and their applications, *Annu Rev Mater Res* **36**:333–368.
58. Fakirov S, Evstatiev M and Petrovich S (1993) Microfibrillar reinforced composites from binary and ternary blends of polyesters and nylon 6, *Macromolecules* **26**:5219–5226.
59. Evstatiev M, Schulz J M, Georgiev G, Petrovich S, Fakirov S and Friedrich K (1998) *In situ* polymer/polymer composites from poly(ethylene terephthalate), polyamide-6, and polyamide-66 blends, *J Appl Polym Sci* **67**:723–737.
60. Fakirov S and Evstatiev M (1994) Microfibrillar reinforced composites – new materials from polymer blends, *Adv Mater* **6**:395–398.
61. Denchev Z, Oliveira M J and Carneiro O S (2004) Nanostructured composites based on polyethylene-polyamide blends: 1. Preparation and mechanical behaviour, *J Macromol Sci Phys* **B43**:143–162.
62. Li Z M, Li L B, Shen K Z, Yang M B and Huang R (2005) *In situ* poly(ethylene terephthalate) microfibers- and shear-induced non-isothermal crystallization of isotactic polypropylene by on-line small angle X-ray scattering, *Polymer* **46**:5358–5367.
63. Dencheva N, Oliveira M J, Carneiro O S, Pouzada A S and Denchev Z (2010) Preparation, structural development, and mechanical properties of microfibrillar composite materials based on PE/PA6 oriented blends, *J Appl Polym Sci* **115**:2918–2932.
64. Dencheva N, Denchev Z, Oliveira M J and Funari S S (2010) Microstructure studies of *in situ* composites based on PE/PA12 blends, *Macromolecules* **43**:4715–4726.
65. Monticciolo A, Cassagnau P and Michel A (1998) Fibrillar morphology development of PE/PBT blends: rheology and solvent permeability, *Polym Eng Sci* **38**:1882–1889.
66. Fakirov S, Bhattacharyya D and Shields R J (2008) Nanofibril reinforced composites from polymer blends, *Colloids Surf A: Physcochem Eng Asp* **313**:2–8.
67. Fasce L, Seltzer R, Frontini P, Rodriguez Pita V J, Pacheco E B A V and Dias M L (2005) Mechanical and fracture characterization of 50:50 HDPE/PET blends presenting different phase morphologies, *Polym Eng Sci* **45:**354–363.
68. Evstatiev O, Oster F, Friedrich K and Fakirov S (2004) On the tribological behavior of microfibrillar reinforced composites from polycondensate-polyolefin blends, *Int J Polym Mater* **53:**1071–1083.
69. Dencheva N, Oliveira M J, Pouzada A S, Kearns M and Denchev Z (2010) Mechanical properties of polyamide 6 reinforced microfibrillar composites, *Polym Comp* (in press).
70. Powell P C (2004) *Engineering with Fiber-Polymer Laminates*, Chapman & Hall, London, UK, p. 113.
71. Palabiyik M and Bahadur S (2000) Mechanical and tribological properties of polyamide 6 and high density polyethylene polyblends with and without compatibilizer, *Wear* **246:**149–158.
72. Dencheva N, Nunes T, Oliveira M J and Denchev Z (2005) Microfibrillar composites based on PE/PA blends; 1 Structure investigations in oriented and isotropic PA6, *Polymer* **46**:887–901.
73. Dencheva N, Denchev Z, Oliveira M J, Nunes T G and Funari S S (2007) Relationship between crystalline structure and mechanical behavior in isotropic and oriented PA6, *J Appl Polym Sci* **103**:2242–2252**.**
74. Nunes P, Pouzada A S and Bernardo CA (2002) The use of a three-point support flexural test to predict the stiffness of anisotropic composite plates in bending, *Polym Testing* **21:**27–33.
75. Pouzada A S and Stevens M J (1984) Methods of generating flexure design data for injection molded plates, *Plast Rubb Proc Appl* **4:**181–187.

76. ABACUS CAE 6.8 version, Copyright 2004 by Dassault Systèmes, USA.
77. Pick L T and Harkin-Jones E (2003) An investigation into the relationship between the impact performance of rotationally molded polyethylene products and their dynamic mechanical properties, *Polym Eng Sci* **43**:905–918.
78. Dencheva N, Denchev Z, Oliveira M J, Nunes T G and Funari S S (2008) Relationship between crystalline structure and mechanical behavior in isotropic and oriented PA12, *J Appl Polym Sci* **109**:288–302.
79. Galanty P G (1999) Nylon 6, in *Polymer Data Handbook* (Ed. Mark J E) Oxford University Press, pp. 180–183.
80. Ulf H and Rohde-Libenau W (1999) Nylon 12, in *Polymer Data Handbook* (Ed. Mark J E) Oxford University Press, pp. 226–227.
81. Quan H, Li Z M, Yang M B and Huang R (2005) On transcrystallinity in semi-crystalline polymer composites, *Compos Sci Technol* **65**:999–1021.
82. Evstatiev M, Nikolov N and Fakirov S (1996) Morphology of microfibrillar reinforced composites PET/PA 6 blend, *Polymer* **37**:4455–4463.
83. Xu H S, Li Z M, Yang S Y, Pan J L, Yang W and Yang M B (2005) Rheological behavior comparison between PET/HDPE and PC/HDPE microfibrillar blends, *Polym Eng Sci* **45**:1231–1238.
84. Nuriel H, Klein N and Marom G (1999) The effect of the transcrystalline layer on the mechanical properties of composite materials in the fiber direction, *Compos Sci Technol* **59**:1685–1690.
85. Sapoundjieva D, Denchev Z, Evstatiev M, Fakirov S, Stribeck N and Stamm M (1999) Transcrystallization with reorientation in drawn PET–PA12 blend as revealed by WAXS from synchrotron radiation, *J Mater Sci* **34**:3063–3066.
86. Fakirov S, Stribeck N, Apostolov A A, Denchev Z, Krasteva B, Evstatiev M and Friedrich K (2001) Crystallization in partially molten oriented blends of polycondensates as revealed by X-ray studies, *J Macromol Sci: Phys* **40**:935–957.
87. Saiello S, Kenny J and Nicolais L (1990) Interface morphology of carbon fiber/PEEK composites, *J Mater Sci* **25**:3493–3496.
88. van Duin M, Aussems M and Borggreve R J M (1998) Graft formation and chain scission in blends of PA6 and PA66 with MAH containing polymers, *J Polym Sci Part A: Polym Chem* **36**:179–188.
89. Thomas S and Groeninckx G (1999) Reactive compatibilisation of heterogeneous ethylene propylene rubber (EPM)/nylon 6 blends by the addition of compatibiliser precursor EPM-g-MA, *Polymer* **40**:5799–5819.
90. Fakirov S, Bhattacharyya D, Lin R J T, Fuchs C and Friedrich K (2007) Contribution of coalescence to microfibril formation in polymer blends during cold drawing, *J Macromol Sci Part B: Phys* **46**:183–194.
91. Perilla J E and Jana S C (2004) A time-scale approach for analysis of coalescence in processing flows, *Polym Eng Sci* **44**:2254–2265.
92. Feldman A Y, Gonzalez M F, Wachtel E, Moret M P and Marom G (2004) Transcrystallinity in aramid and carbon fiber reinforced PA66: determining the lamellar orientation by synchrotron X-ray microdiffraction, *Polymer* **45**:7239–7245.
93. Harel H and Marom G (1998) On the crystalline interfaces in composite materials, *Acta Polymerica* **49**:583–587.
94. Klein N, Marom G and Wachtel E (1996) Microstructure of PA66 transcrystalline layers in carbon and aramid fiber reinforced composites, *Polymer* **37**:5493–5498.
95. Stern T, Wachtel E and Marom G (1997) Epitaxy and lamellar twisting in transcrystalline PE, *J Polym Sci Polym Phys* **35**:2429–2433.

96. Stern T, Marom G and Wachtel E (1997) Origin, morphology and crystallography of transcrystallinity in PE-based single polymer composites, *Compos Part A Appl S* **28**:437–444.
97. Zhang S, Minus M L, Zhu L, Wong C-P and Kumar S (2008) Polymer transcrystallinity induced by carbon nanotubes, *Polymer* **49**:1356–1364.
98. Hernández J J, García-Gutiérrez M C, Nogales A, Rueda D R, Sanz A, Sics I, Hsiao B S, Roslaniec Z, Broza G and Ezquerra T A (2007) Deformation behavior during cold drawing of nanocomposites based on single wall carbon nanotubes and poly(ether ester) copolymers, *Polymer* **48**:3286–3293.
99. Nogales A, Hsiao B S, Somani R H, Srinivas S, Tsou A H, Balta-Calleja F J and Ezquerra T A (2001) Shear-induced crystallization of isotactic polypropylene with different molecular weight distributions: *in situ* small- and wide-angle X-ray scattering studies, *Polymer* **42**:5247–5256.
100. Polar Software, Version 2.7.1; Stonybrook Technology and Applied Research, New York, 2008.
101. Dencheva N, Nunes T, Oliveira M J and Denchev Z (2005) Crystalline structure of polyamide 12 as revealed by solid-state ^{13}C NMR and synchrotron WAXS and SAXS, *J Polym Sci Part B: Polym Phys* **43**:3720–3733.
102. Stribeck N (2010) X-ray scattering for the monitoring of processes in polymer materials with fiber symmetry, *Polym Rev* **50**:40–58.
103. Stribeck N (2001) Extraction of domain structure information from SAXS patterns of bulk materials, *J Appl Cryst* **34**:496–503.
104. Denchev Z, Dencheva N, Funari S S, Motovilin M, Schubert T and Stribeck N (2010) Nanostructure and mechanical properties studied during dynamical straining of microfibrillar reinforced HDPE/PA blends, *J Polym Sci: Part B: Polym Phys* **48**:237–250.
105. Stribeck N (2007) *X-Ray Scattering of Soft Matter*, Springer Verlag, Berlin Heidelberg, Germany, Ch. 1, p. 8.